An adjoint-based optimization method for jointly inverting heterogeneous material properties and fault slip from earthquake surface deformation data

S. Puel[1,2], T. W. Becker[1,2,3], U. Villa[3], O. Ghattas[3,4], and D. Liu[2]

[1] *Department of Geological Sciences, Jackson School of Geosciences, The University of Texas at Austin*
[2] *Institute for Geophysics, Jackson School of Geosciences, The University of Texas at Austin*
[3] *Oden Institute for Computational Engineering and Sciences, The University of Texas at Austin*
[4] *Walker Department of Mechanical Engineering, The University of Texas at Austin*

This manuscript is a preprint uploaded to *EarthArXiv*. This preprint has been submitted for publication in *Geophysical Journal International* and has not yet been peer-reviewed. We welcome feedback, discussion, and comments at any time. Feel free to get in touch with one of the authors.

Corresponding author: **Simone Puel**
Email: spuel@utexas.edu

submitted to *Geophys. J. Int.*

An adjoint-based optimization method for jointly inverting heterogeneous material properties and fault slip from earthquake surface deformation data

S. Puel[1,2⋆], T. W. Becker[1,2,3], U. Villa[3], O. Ghattas[3,4], and D. Liu[2]

[1] *Department of Geological Sciences, Jackson School of Geosciences, The University of Texas at Austin, Austin, TX 78712, USA*

[2] *Institute for Geophysics, Jackson School of Geosciences, The University of Texas at Austin, Austin, TX 78712, USA*

[3] *Oden Institute for Computational Engineering & Sciences, The University of Texas at Austin, Austin, TX 78712, USA*

[4] *Walker Department of Mechanical Engineering, The University of Texas at Austin, Austin, TX 78712, USA*

SUMMARY

Analysis of tectonic and earthquake-cycle associated deformation of the crust can provide valuable insights into the underlying deformation processes including fault slip. How those processes are expressed at the surface depends on the lateral and depth variations of rock properties. The effect of such variations is often tested by forward models based on *a priori* geological or geophysical information. Here, we first develop a novel technique based on an open-source finite-element computational framework to invert geodetic constraints directly for heterogeneous media properties. We focus on the elastic, coseismic problem and seek to constrain variations in shear modulus and Poisson's ratio, proxies for the effects of lithology and/or temperature and porous flow, respectively. The corresponding non-linear inversion is implemented using adjoint-based optimization that efficiently reduces the cost functional that includes the misfit between the calculated and observed displacements and a penalty term. We then extend our theoretical and numerical framework to simultaneously infer both heterogeneous Earth's structure and fault slip from

surface deformation. Based on a range of 2-D synthetic cases, we find that both model parameters can be satisfactorily estimated for the megathrust setting-inspired test problems considered. Within limits, this is the case even in the presence of noise and if the fault geometry is not perfectly known. Our method lays the foundation for a future reassessment of the information contained in increasingly data-rich settings, e.g. geodetic GNSS constraints for large earthquakes such as the 2011 Tohoku-oki M9 event, or distributed deformation along plate boundaries as constrained from InSAR.

Key words: Seismic cycle; Inverse theory; Joint inversion; Numerical modelling; Earthquake source observations; Kinematics of crustal and mantle deformation.

1 INTRODUCTION

Crustal displacement time series, e.g. as recorded by the Global Navigation Satellite System (GNSS) or Interferometric Synthetic Aperture Radar (InSAR), contain information about both Earth structure and the drivers of deformation, such as earthquakes within the seismic cycle. Depending on the questions asked, heterogeneity in the Earth may be signal or nuisance. For example, for the elastic problem of inverting surface deformation for fault slip or plate boundary loading for megathrust margins, material heterogeneity such as lateral variations in shear moduli due to sediment cover can affect fault slip inversions (e.g., Williams & Wallace 2015, 2018; Hashima et al. 2016). Other effects of lateral material variations in subduction zones can be due to the presence of the volcanic arc, for example (e.g., Takada & Fukushima 2013; Muto et al. 2016; Dhar et al. 2022). Exploring such effects usually involves computing different linear coseismic slip inversions and adjusting the Earth structure model, e.g. based on information from other geophysical or geological constraints. However, to comprehensively explore the contributions of fault slip uncertainty and material variations, it is necessary to analyze the trade-off between these parameters, preferably by jointly inverting the surface deformation for fault slip and structural heterogeneity.

The accurate inference of Earth's structure given imperfect sampling and trade-offs is, of course, a long-standing challenge in geosciences. Material properties at depth are often inferred from variations in seismic wave speeds. However, uncertainties arise when converting seismic velocities and/or attenuation properties to elastic and viscous moduli due to factors such as temperature, volatile content,

⋆ Email: spuel@utexas.edu

and composition. To reduce the resulting non-uniqueness in tectonic settings, a range of studies have explored joint inversions using different deformation constraints (e.g., Reuber 2021).

Standard inverse approaches like grid search or sampling-based techniques (Baumann et al. 2014) may allow consideration of different constraints but are computationally expensive due to the non-linear scaling of required forward models with the number of model parameters and data dimensions (Reuber et al. 2020). Gradient-based methods, on the other hand, are more efficient as the numerical cost is often independent of the number of parameters to recover (Reuber et al. 2020). The gradient of the objective function, composed of the data misfit and a regularization term, can be evaluated through numerical and analytic differentiation or using the adjoint method (e.g., Bonnet & Constantinescu 2005; Avril et al. 2008; Reuber 2021). The latter is particularly efficient for accurately computing the gradient and can also be used to compute the second-order derivative, known as the Hessian, which is useful for convergence acceleration and uncertainty quantification (e.g., Kelley & Sachs 1991; Martin et al. 2012; Petra et al. 2014; Bui-Thanh & Ghattas 2015; Isaac et al. 2015; Ghattas & Willcox 2021).

Commonly, such studies utilize adjoint-based optimization methods to efficiently solve linear/non-linear inverse problems, and adjoint approaches are increasingly used for mantle convection problems (e.g., Bunge et al. 2003; Liu & Gurnis 2008; Worthen et al. 2014; Reuber et al. 2020; Rudi et al. 2022). In the seismotectonic context, Crawford et al. (2017) employed viscoelastic models and adjoints to invert surface deformations after earthquakes and recover the viscosity structure in 2-D synthetic tests. Agata et al. (2017) used adjoints to invert surface geodetic velocities to recover both the afterslip distribution and a three-layered asthenosphere viscosity structure beneath Japan.

However, the accurate and efficient implementation of first and second derivatives in numerical models remains a challenge. Previous studies have addressed this challenge by representing the model domain with finite-element or finite-difference schemes and deriving the adjoint equation based on this discretization (Crawford et al. 2017; Agata et al. 2017; Reuber et al. 2020). However, this approach is problem-specific, requiring manual modification of the discretization for each problem, and can make the derivation of the discrete Hessian very difficult, particularly for complex discretizations of constitutive laws (Ghattas & Willcox 2021; Villa et al. 2021).

Recent developments in advanced open-source libraries have addressed the issues of flexibility and optimization in both mesh discretization and solver options (Balay et al. 2020), enhancing the solution of complex multiphysics coupling problems (e.g., Logg & Wells 2010; Wilson et al. 2017; Rathgeber et al. 2016; Villa et al. 2021). In particular, the hIPPYLIB library (Villa et al. 2018, 2021) relies on FENICS (Logg & Wells 2010; Logg et al. 2012) for the finite-element discretization, and implements state-of-the-art scalable adjoint-based algorithms for PDE-based deterministic and Bayesian inverse problems. In hIPPYLIB, both gradient and Hessian information of the objective function are

efficiently computed using the adjoint method while leveraging the automated symbolic differentiation and assembly of variational forms in FENICS (Alnæs et al. 2014). This makes the solution of any PDE-based inverse problem transparent and relatively straightforward, overcoming challenges associated with problem-specific implementations.

Here, we aim to utilize these powerful libraries to address the problem of inferring Earth's material heterogeneity based on surface geodetic observations during large earthquakes. Previous related efforts have focused on recovering elastic properties for engineering problems with sparse observations throughout the domain (Fatehiboroujeni et al. 2016, 2020). However, these models were limited to solving simple 2-D tests with constraints impossible to achieve for solid Earth problems, where geodetic data is limited to the surface. In this paper, we seek to investigate for the first time, to our knowledge, if surface geodetic data alone can provide sufficient information about both the fault slip distribution and Earth's structure for subduction earthquake type problems.

Puel et al. (2022) described a novel fault discontinuity implementation in finite-element (FE) modeling using a stress-accurate mixed FE elastic formulation and discussed formal links between linear coseismic slip inversion and adjoint-based optimization methods, which eliminate the need for Green's function computations. Here, we build upon this computational framework, leveraging the capabilities of FENICS and HIPPYLIB. First, we review the elastic forward model, and then we formulate and derive expressions for the gradient and Hessian of the infinite-dimensional deterministic nonlinear inverse problem for heterogeneous material property distribution (e.g., Poisson's ratio), and present numerical results for inversion in the crust and mantle wedge in sections 2 and 3, respectively. Lastly, in section 4, we extend our work by combining the fault slip inversion presented in Puel et al. (2022) with the inference of heterogeneous material properties, specifically variations in the shear modulus, for a joint inversion to infer both model parameters. A 3-D application of this approach involving actual coseismic surface GNSS data is beyond the scope of this work and will be addressed in a separate manuscript.

2 FORWARD PROBLEM: ELASTICITY MIXED FORMULATION

Given any point $\boldsymbol{x}$ within the domain $\Omega \subset \mathbb{R}^d, d = 2, 3$ with Dirichlet (Γ_D) and Neumann (Γ_N) external boundaries, and an internal fault discontinuity Γ_F, the Hellinger-Reissner formulation of the elasticity equation aims to find the displacement $\boldsymbol{u}$, stress $\boldsymbol{\sigma}$, and rotation $\boldsymbol{\varrho}$ fields that satisfy the governing equations (Arnold et al. 2007) and the fault and external boundary conditions (Puel et al.

2022):

$$\begin{cases} \boldsymbol{A\sigma} = \nabla \boldsymbol{u} - \boldsymbol{\varrho} & \text{in } \Omega, \\ -\nabla \cdot \boldsymbol{\sigma} = \boldsymbol{f} & \text{in } \Omega, \\ \boldsymbol{u} = \boldsymbol{u}_0 & \text{on } \Gamma_D, \\ \boldsymbol{\sigma} \cdot \mathbf{n} = \boldsymbol{t} & \text{on } \Gamma_N, \\ [\![T(\mathbf{n}_{\Gamma_F})\boldsymbol{u}]\!] = \boldsymbol{s} & \text{on } \Gamma_F, \\ [\![\boldsymbol{u} \cdot \mathbf{n}_{\Gamma_F}]\!] = 0 & \text{on } \Gamma_F, \\ [\![\boldsymbol{\sigma} \cdot \mathbf{n}_{\Gamma_F}]\!] = \mathbf{0} & \text{on } \Gamma_F, \end{cases} \tag{1}$$

where we write the strain tensor as the difference between $\nabla \boldsymbol{u}$ and its skew-symmetric part $\boldsymbol{\varrho} = \frac{1}{2}(\nabla \boldsymbol{u} - \nabla \boldsymbol{u}^T)$. The first and second equations represent the constitutive relation and linear balance of momentum, respectively. Here, $\boldsymbol{A} = \boldsymbol{A}(\boldsymbol{x})$ is the fourth-order elastic compliance tensor describing the material properties of the medium, $\boldsymbol{r}$ the skew-symmetric part of the gradient deformation tensor $\nabla \boldsymbol{u}$, $\boldsymbol{f}$ represents body forces, $\boldsymbol{u}_0$ is the imposed displacement at the boundaries, $\mathbf{n}$ denotes the outward unit normal of $\partial\Omega$, and $\boldsymbol{t}$ is the traction. The last three conditions in eq. (1) represent the constraints on the fault discontinuity (Puel et al. 2022). $[\![\boldsymbol{\theta}]\!] = \boldsymbol{\theta}^- - \boldsymbol{\theta}^+$ is the jump operator that restricts the function $\boldsymbol{\theta}$ from the left, $\boldsymbol{\theta}^-$, and right, $\boldsymbol{\theta}^+$, side of the fault respectively. $T(\mathbf{n}_{\Gamma_F})$ is the tangent operator which takes the component of the displacement $\boldsymbol{u}$ parallel to the fault plane Γ_F. $\boldsymbol{s}$ is the fault slip and $\mathbf{n}_{\Gamma_F} = \mathbf{n}^+ = -\mathbf{n}^-$ is the unit vector normal to Γ_F. For an isotropic, linear-elastic medium, the compliance $\boldsymbol{A}(\boldsymbol{x})$ depends only on two independent scalar fields: e.g., the shear modulus $\mu(\boldsymbol{x})$ and second Lamé parameter $\lambda(\boldsymbol{x})$, or $\mu(\boldsymbol{x})$ and the Poisson's ratio $\nu(\boldsymbol{x})$ (Appendix A)

$$\boldsymbol{A\sigma} = \frac{1}{2\mu}\left[\boldsymbol{\sigma} - \frac{\nu}{1+\nu(d-2)}\mathrm{tr}(\boldsymbol{\sigma})\boldsymbol{I}\right], \tag{2}$$

where $\boldsymbol{I}$ is the $d \times d$ identity matrix and $\mathrm{tr}(\boldsymbol{\sigma})$ is the trace of the stress tensor.

Following Arnold et al. (2007), we employ a mixed FE method to discretize the three spatial fields. In this approach, the stress is approximated using Brezzi-Douglas-Marini H(div)-conforming finite elements (Brezzi et al. 1985). These elements are piece-wise vector polynomials on each mesh element and have continuous normal components across inter-element facets. The displacement and rotation fields are approximated by piece-wise discontinuous Galerkin elements. This mixed FE discretization satisfies stress balance discretely and provides a higher order of accuracy for the stress variable than the standard displacement elastic formulation (Puel et al. 2022). Another advantage of using a discontinuous Galerkin discretization for the displacement field is that the slip can be prescribed across the fault without the need of conventional split node (Melosh & Raefsky 1981) or decomposition discrete approaches (Aagaard et al. 2013).

Hence, the elasticity equation in this mixed FE approximation seeks to find $(\boldsymbol{\sigma}_h, \boldsymbol{u}_h, \boldsymbol{r}_h) \in \Sigma_h \times$

$W_h \times \Xi_h$, where $\boldsymbol{r}_h = \frac{1}{2}\nabla \times \boldsymbol{u}$ is the rotation vector of the skew symmetric tensor $\boldsymbol{\varrho}$, such that

$$\begin{aligned}
\int_{\Omega_h} \boldsymbol{A}\boldsymbol{\sigma}_h : \boldsymbol{\tau}_h \,\mathrm{d}\boldsymbol{x} + \int_{\Omega_h} \boldsymbol{u}_h \cdot (\nabla \cdot \boldsymbol{\tau}_h)\,\mathrm{d}\boldsymbol{x} + \int_{\Omega_h} \mathrm{as}(\boldsymbol{\tau}_h) \cdot \boldsymbol{r}_h \,\mathrm{d}\boldsymbol{x} \\
= \int_{\Gamma_{h,F}} \boldsymbol{s} \cdot \left[T(\mathbf{n}_{\Gamma_F})(\boldsymbol{\tau}_h\, \mathbf{n}_{\Gamma_F})\right] \mathrm{d}\boldsymbol{S} \quad \forall \boldsymbol{\tau}_h \in \Sigma_h, \\
-\int_{\Omega_h} (\nabla \cdot \boldsymbol{\sigma}_h) \cdot \boldsymbol{\omega}_h \,\mathrm{d}\boldsymbol{x} = \int_{\Omega_h} \boldsymbol{f} \cdot \boldsymbol{\omega}_h \,\mathrm{d}\boldsymbol{x} \quad \forall \boldsymbol{\omega}_h \in W_h, \\
\int_{\Omega_h} \mathrm{as}(\boldsymbol{\sigma}_h) \cdot \boldsymbol{\xi}_h \,\mathrm{d}\boldsymbol{x} = 0 \quad \forall \boldsymbol{\xi}_h \in \Xi_h,
\end{aligned} \tag{3}$$

where Ω_h and $\Gamma_{h,F}$ are the discretized domain and the union of facets aligning with the fault geometry, respectively. Here, $\mathrm{as}(\boldsymbol{\tau}) = (\tau_{12} - \tau_{21})$ and $\mathrm{as}(\boldsymbol{\tau}) = (\tau_{32} - \tau_{23}, \tau_{13} - \tau_{31}, \tau_{21} - \tau_{12})^T$ is the asymmetric operator in 2-D and 3-D, respectively. $\boldsymbol{\tau}_h, \boldsymbol{\omega}_h, \boldsymbol{\xi}_h$ are the test functions for stress, displacement and rotation, respectively, and $\mathrm{d}\boldsymbol{S}$ represents the integration over the fault internal boundary. The discretized spaces are defined as $\Sigma_h = \{\boldsymbol{\tau} \in H(\nabla\cdot, \Omega_h, \mathbb{M}) : \boldsymbol{\tau}\,\mathbf{n} = \mathbf{0} \text{ on } \Gamma_{h,N}, [\![\boldsymbol{\tau}\,\mathbf{n}_{\Gamma_F}]\!] = \mathbf{0} \text{ on } \Gamma_{h,F}\}$, $W_h = L^2(\Omega_h, \mathbb{R}^d)$, $\Xi_h = L^2(\Omega_h, \mathbb{R}^d)$, which respectively represent the space of square-integrable matrix fields with square-integrable divergence satisfying the traction and fault boundary conditions, and the spaces of all square-integrable vector fields. The restriction on the stress space along $\Gamma_{h,F}$ is effectively satisfied when the fault is resolved by the computational grid. $\Gamma_{h,N}$ is the discretized external boundaries. The discretization details including the fault derivation from the integration by parts of the non-conforming term in the constitutive equation can be found in Puel et al. (2022).

3 INFINITE-DIMENSIONAL DETERMINISTIC INVERSION FOR POISSON'S RATIO

In this section we derive the formulation in infinite dimensions—i.e. at a continuous integral level—of the deterministic inverse problem for heterogeneous medium properties using the FE method. Here, we choose to invert for the Poisson's ratio which has been used as a proxy for the presence of fluids in the mantle wedge and postseismic poroelastic effects (e.g., Feigl & Thatcher 2006; Panuntun et al. 2018). An analogous procedure will be employed in section 4 to jointly invert surface deformation for both the shear modulus field and fault slip.

Given an infinite-dimensional Hilbert space of functions $\mathcal{M}$ defined on the domain Ω, and some sparse noisy finite-dimensional surface deformation observations $\mathbf{d} \in \mathbb{R}^{n_{\mathrm{obs}}}$, we seek to infer the Poisson's ratio field $\nu(\boldsymbol{m}) = \frac{1}{4}[1 + \tanh(\boldsymbol{m})]$ which best predicts the data. The choice of inverting for the argument of the hyperbolic tangent $\boldsymbol{m} \in \mathcal{M}$ derives from the physical constraints of the Poisson's ratio, $\nu \in [0, 0.5]$. We formulate this non-linear inverse problem as the following constrained least-

squares optimization problem:

$$\min_{\boldsymbol{m}\in\mathcal{M}} \mathcal{J}(\boldsymbol{m}) := \frac{1}{2}||\mathcal{F}(\boldsymbol{m}) - \mathbf{d}||^2_{\boldsymbol{\Gamma}^{-1}_{\text{noise}}} + \mathcal{R}(\boldsymbol{m}), \tag{4}$$

where the cost functional $\mathcal{J}(\boldsymbol{m})$ contains the data misfit, weighted by the data noise covariance $\boldsymbol{\Gamma}^{-1}_{\text{noise}}$, and a regularization term $\mathcal{R}(\boldsymbol{m})$, respectively. The latter term is necessary due to the ill-posedness of most inverse problems (e.g., Hadamard 1923; Tikhonov & Arsenin 1977). $\mathcal{F}(\boldsymbol{m}) := \mathcal{B}\boldsymbol{u}(\boldsymbol{m})$ is the parameter-to-observable map and $\boldsymbol{u}(\boldsymbol{m})$ is the displacement field computed by solving the elasticity problem (eq. 3) given the Poisson's ratio parameter field $\boldsymbol{m}$. $\mathcal{B}$ is an observation operator restricting the predicted displacement field to the surface observations.

For the case of material properties inference, $\boldsymbol{u}$ depends on $\boldsymbol{m}$ non-linearly. Therefore, we seek to find an efficient and scalable algorithm to solve this minimization problem (eq. 4). Newton's method proves to be suitable for this purpose by providing a fast and efficient solution of the discretized infinite-dimensional optimization problem (e.g., Allgower et al. 1986; Heinkenschloss 1993). By leveraging information from the second derivative of the least-squares cost functional (the Hessian), these methods have demonstrated mesh-independent convergence (e.g., Kelley & Sachs 1991; Ghattas & Willcox 2021), requiring significantly fewer forward PDE solves than algorithms relying only on gradient information.

Newton's method requires the computation of the (infinite-dimensional) gradient and Hessian, which are the first and second-order Gâteaux derivatives of the objective function $\mathcal{J}(\boldsymbol{m})$ with respect to $\boldsymbol{m}$. Gradient and Hessian expressions can be derived through variational calculus and the adjoint method. Using the Lagrangian formalism (Tröltzsch 2010) we formulate an expression for the gradient $\mathcal{G}(\boldsymbol{m})$ at an arbitrary point $\boldsymbol{m}^*$ in parameter space. The Lagrangian functional for the gradient $\mathcal{L}^{\mathcal{G}}$ includes eq. (4) and the weak form of the forward problem (eq. 3),

$$\mathcal{L}^{\mathcal{G}}(\boldsymbol{\phi}, \boldsymbol{m}, \boldsymbol{p}) = \frac{1}{2}||\mathcal{B}\boldsymbol{u}(\boldsymbol{m}) - \mathbf{d}||^2_{\boldsymbol{\Gamma}^{-1}_{\text{noise}}} + \mathcal{R}(\boldsymbol{m}) + \int_\Omega \boldsymbol{p}\cdot\boldsymbol{\psi}(\boldsymbol{\phi}, \boldsymbol{m})\,\mathrm{d}\boldsymbol{x}, \tag{5}$$

where $\boldsymbol{\phi} = (\boldsymbol{\sigma}, \boldsymbol{u}, \boldsymbol{r})$ and $\boldsymbol{p} = (\boldsymbol{\tau}, \boldsymbol{\omega}, \boldsymbol{\xi})$ are the state and adjoint variables where the latter serve as Lagrange multipliers for the stress, displacement and rotation, respectively. $\boldsymbol{\psi}(\boldsymbol{\phi}, \boldsymbol{m})$ is the residual of the elasticity PDE (eq. 1). The second term, $\mathcal{R}(\boldsymbol{m})$, could be for example a Tikhonov-type regularization that imposes a certain level of smoothness of the solution $\boldsymbol{m}$.

By taking the derivative of $\mathcal{L}^{\mathcal{G}}$ with respect to the adjoint and state variables we obtain the varia-

tional form of the forward and adjoint equations, respectively. The latter reads:

$$\begin{aligned}\left(\frac{\partial \mathcal{L}^{\mathcal{G}}}{\partial \boldsymbol{\sigma}}, \tilde{\boldsymbol{\sigma}}\right) + \left(\frac{\partial \mathcal{L}^{\mathcal{G}}}{\partial \boldsymbol{u}}, \tilde{\boldsymbol{u}}\right) + \left(\frac{\partial \mathcal{L}^{\mathcal{G}}}{\partial \boldsymbol{r}}, \tilde{\boldsymbol{r}}\right) = &\int_\Omega \frac{1}{2\mu}\big[\tilde{\boldsymbol{\sigma}} - \frac{\nu(\boldsymbol{m})}{1+\nu(\boldsymbol{m})(d-2)}\operatorname{tr}(\tilde{\boldsymbol{\sigma}})\boldsymbol{I}\big] : \boldsymbol{\tau}\,\mathrm{d}\boldsymbol{x} \\ &+ \int_\Omega (\nabla\cdot\tilde{\boldsymbol{\sigma}})\cdot\boldsymbol{\omega}\,\mathrm{d}\boldsymbol{x} + \int_\Omega \operatorname{as}(\tilde{\boldsymbol{\sigma}})\cdot\boldsymbol{\xi}\,\mathrm{d}\boldsymbol{x} \\ &+ \int_\Omega \tilde{\boldsymbol{u}}\cdot(\nabla\cdot\boldsymbol{\tau})\,\mathrm{d}\boldsymbol{x} + \int_\Omega \operatorname{as}(\boldsymbol{\tau})\cdot\tilde{\boldsymbol{r}}\,\mathrm{d}\boldsymbol{x} \\ &+ \int_\Omega \mathcal{B}^*\boldsymbol{\Gamma}_{\text{noise}}^{-1}\big(\mathcal{B}\boldsymbol{u} - \mathbf{d}\big)\cdot\tilde{\boldsymbol{u}}\,\mathrm{d}\boldsymbol{x} = 0 \\ &\forall\tilde{\boldsymbol{\sigma}}\in\Sigma;\ \forall\tilde{\boldsymbol{u}}\in W;\ \forall\tilde{\boldsymbol{r}}\in\Xi,\end{aligned} \tag{6}$$

where $\mathcal{B}^*$ is the adjoint of the observational operator which maps the discrete surface displacement back to the infinite-dimensional state space, and $\tilde{\boldsymbol{\sigma}}$, $\tilde{\boldsymbol{u}}$, and $\tilde{\boldsymbol{r}}$ are test functions.

By taking a variation of the Lagrangian functional with respect to the model parameter, we obtain the pointwise gradient expression at a point $\boldsymbol{m}^*$ in an arbitrary direction $\tilde{\boldsymbol{m}}$:

$$(\mathcal{G}(\boldsymbol{m}^*), \tilde{\boldsymbol{m}}) = (\mathcal{R}_m(\boldsymbol{m}^*), \tilde{\boldsymbol{m}}) - \frac{1}{E}\int_\Omega \frac{\nu_m(\boldsymbol{m}^*)\,\tilde{\boldsymbol{m}}}{\big[1+\nu(\boldsymbol{m}^*)(d-2)\big]^2}\operatorname{tr}(\boldsymbol{\sigma})\boldsymbol{I} : \boldsymbol{\tau}\,\mathrm{d}\boldsymbol{x} \qquad \forall\tilde{\boldsymbol{m}}\in\mathcal{M}, \tag{7}$$

where $(\mathcal{R}_m(\boldsymbol{m}^*), \tilde{\boldsymbol{m}})$ denotes the Gâteaux derivative of the regularization $\mathcal{R}$ with respect to $\boldsymbol{m}$ in the direction $\tilde{\boldsymbol{m}}$ evaluated at $\boldsymbol{m} = \boldsymbol{m}^*$. $\nu_m(\boldsymbol{m})$ indicates the derivative of $\nu(\boldsymbol{m})$ with respect to $\boldsymbol{m}$. $\boldsymbol{\sigma}$ and $\boldsymbol{\tau}$ are the solutions of the forward and adjoint problems (eqs. 1 and 6), respectively. The cost of evaluating the gradient consists of one forward and one adjoint PDE solve.

Eq. (1) shows that $\boldsymbol{u}$ depends on $\boldsymbol{m}$ in a nonlinear manner through the solution of the forward mixed elasticity problem. Therefore, we can leverage Hessian information in combination with Newton's method to accelerate the convergence of the Poisson's ratio inference. For the derivation of the Hessian action in a direction $\hat{\boldsymbol{m}}$ in parameter space, we follow the same approach as before and construct the second-order Lagrangian functional $\mathcal{L}^{\mathcal{H}}$, which consists of the sum of the gradient, forward equation (second term), and adjoint equation (last two terms), respectively:

$$\begin{aligned}\mathcal{L}^{\mathcal{H}}(\boldsymbol{\phi}, \boldsymbol{m}, \boldsymbol{p}; \hat{\boldsymbol{\phi}}, \hat{\boldsymbol{m}}, \hat{\boldsymbol{p}}) = &(\mathcal{G}(\boldsymbol{m}), \hat{\boldsymbol{m}}) + \int_\Omega \hat{\boldsymbol{p}}\cdot\boldsymbol{\psi}(\boldsymbol{\phi}, \boldsymbol{m})\,\mathrm{d}\boldsymbol{x} \\ &+ \int_\Omega \boldsymbol{p}\cdot\boldsymbol{\psi}_\phi(\boldsymbol{\phi}, \boldsymbol{m})[\hat{\boldsymbol{\phi}}]\,\mathrm{d}\boldsymbol{x} + \int_\Omega \mathcal{B}^*\boldsymbol{\Gamma}_{\text{noise}}^{-1}\big(\mathcal{B}\boldsymbol{u} - \mathbf{d}\big)\cdot\hat{\boldsymbol{u}}\,\mathrm{d}\boldsymbol{x},\end{aligned} \tag{8}$$

where $\hat{\boldsymbol{\phi}}, \hat{\boldsymbol{m}}, \hat{\boldsymbol{p}}$ are the test functions of the forward, gradient, and adjoint equations, respectively. $\boldsymbol{\psi}_\phi$ is the derivative of the forward PDE residual with respect to the state variables. To obtain the action of

the Hessian in a direction $\hat{\boldsymbol{m}}$ we take the variation of $\mathcal{L}^{\mathcal{H}}$ with respect to $\boldsymbol{m}$:

$$
\begin{aligned}
(\tilde{\boldsymbol{m}}, \mathcal{H}(\boldsymbol{m})\,\hat{\boldsymbol{m}}) = (\tilde{\boldsymbol{m}}, \mathcal{R}_{mm}(\boldsymbol{m})\,\hat{\boldsymbol{m}}) \\
- \frac{1}{2\mu}\int_\Omega \frac{\left[\nu_{mm}(\boldsymbol{m}) + 2\nu_m^2(\boldsymbol{m})(d-2)\right]}{\left[1+\nu(\boldsymbol{m})(d-2)\right]^2}\,\tilde{\boldsymbol{m}}\hat{\boldsymbol{m}}\,\mathrm{tr}(\boldsymbol{\sigma})\boldsymbol{I} : \boldsymbol{\tau}\,\mathrm{d}\boldsymbol{x} \\
- \frac{1}{2\mu}\int_\Omega \frac{\nu_m(\boldsymbol{m})\,\tilde{\boldsymbol{m}}}{\left[1+\nu(\boldsymbol{m})(d-2)\right]^2}\left[\mathrm{tr}(\boldsymbol{\sigma})\boldsymbol{I} : \hat{\boldsymbol{\tau}} + \mathrm{tr}(\hat{\boldsymbol{\sigma}})\boldsymbol{I} : \boldsymbol{\tau}\right]\mathrm{d}\boldsymbol{x} \qquad \forall \tilde{\boldsymbol{m}} \in \mathcal{M},
\end{aligned}
\tag{9}
$$

where ν_m and ν_{mm} denote the first and second derivatives of $\nu(\boldsymbol{m})$ with respect to $\boldsymbol{m}$, respectively. $\boldsymbol{\sigma}$ and $\boldsymbol{\tau}$ are the solutions to the forward and adjoint problems in eqs. (1) and (6), respectively, and $\hat{\boldsymbol{\sigma}}$ and $\hat{\boldsymbol{\tau}}$ are the solutions of the incremental forward and adjoint problems, respectively (see Appendix B). Once we have gradient and Hessian action expressions, we can apply an inexact Newton-conjugate gradient (Newton-CG) algorithm (e.g., Akçelik et al. 2006; Borzì & Schulz 2011) to solve the optimization problem in eq. (4). At each kth Newton iteration, we solve the linear system,

$$
\mathcal{H}(\boldsymbol{m}_k)\,\hat{\boldsymbol{m}}_k = -\mathcal{G}(\boldsymbol{m}_k), \tag{10}
$$

for the Newton direction $\hat{\boldsymbol{m}}_k$ with the linear CG method in a matrix-free manner via a pair of incremental forward/adjoint PDE solves, terminating early to avoid negative curvature and over-solving (Steihaug 1983; Eisenstat & Walker 1996). The search direction solution provides an update to the model parameter $\boldsymbol{m}_{k+1}$ at the $(k+1)$th iteration as

$$
\boldsymbol{m}_{k+1} = \boldsymbol{m}_k + \alpha_k\,\hat{\boldsymbol{m}}_k, \tag{11}
$$

with asymptotic quadratic convergence. The step length $\alpha_k \in (0, 1]$ is chosen according to an appropriate line search strategy (e.g., Nocedal & Wright 1999). The advantages of this inexact Newton-CG algorithm are: 1) The Hessian operator is not built explicitly because the operator-free CG algorithm requires only the matrix action on a given vector via eq. (9); 2) the cost per Newton iteration of solving eq. (10) involves a pair of linearized PDE solves, one incremental forward and one incremental adjoint problem; and 3) the number of iterations for convergence does not depend on the parameter or the nominal data dimension (e.g., Ghattas & Willcox 2021; Villa et al. 2021). The computational cost, measured in linearized PDE solves, depends only on the intrinsic dimensionality of the problem—i.e. the number of directions in parameter space that are informed by the data. HIPPYLIB does not require the direct input of the gradient and Hessian expressions, but only the variational form of the forward problem (eq. 3), automatically computing the gradient and Hessian action using the symbolic differentiation capabilities of the FENICS library. In the following section we will focus on the regularization term $\mathcal{R}(\boldsymbol{m})$ in the context of the heterogeneous Poisson's ratio inference from surface deformation data.

3.1 Tikhonov vs. Total Variation (TV) regularization

In the absence of the regularization term $\mathcal{R}(\boldsymbol{m})$, solving the optimization problem stated in eq. (4) becomes challenging. In typical cases where $\mathcal{F}(\mathbf{m})$ is governed by PDEs with infinite-dimensional parameters, the inverse problem is ill-posed—i.e. its solution, if it exists, is not unique and is highly sensitive to errors in the data and model (e.g., Hadamard 1923; Engl et al. 1996; Vogel 2002).

A common feature of many ill-posed inverse problems is the rapid decay of the spectrum of the Hessian of the data fidelity term. The inverse of the Hessian's small eigenvalues amplify noise components contained in the data in the directions of the corresponding eigenfunctions, leading to unstable inference of these modes. The faster the decay of the spectrum of the Hessian and the higher the noise, the fewer eigenvalues will be above the noise level, and the fewer modes of $\mathbf{m}$ can be reliably recovered from the data (Ghattas & Willcox 2021). Since the data are not sensitive to eigenfunction modes associated with these smaller eigenvalues, we may remove them by truncating the spectrum—i.e. truncated singular value decomposition. However, this approach is applicable only when $\mathcal{F}(\boldsymbol{m})$ is a linear operator. A more general strategy, also for non-linear operators, is to use some type of regularization $\mathcal{R}(\boldsymbol{m})$ (e.g., Arridge et al. 2019; Benning & Burger 2018) such as Tikhonov regularization (Tikhonov 1963; Tikhonov & Arsenin 1977), which, acting as a filter, damps the smallest eigenvalues.

Perhaps the most popular type of Tikhonov regularization is the H^1 norm, which penalizes oscillatory components of the gradient of the model parameter $\boldsymbol{m}$ by imposing smoothness:

$$\mathcal{R}^{H^1}(\boldsymbol{m}) = \frac{\gamma_{H^1}}{2}\int_\Omega \nabla\boldsymbol{m}\cdot\nabla\boldsymbol{m}\,\mathrm{d}\boldsymbol{x} + \frac{\delta_{L^2}}{2}\int_\Omega \boldsymbol{m}\cdot\boldsymbol{m}\,\mathrm{d}\boldsymbol{x}, \tag{12}$$

where γ_{H^1} acts as a diffusion coefficient that controls the strength of the penalty. This parameter is usually chosen by using such techniques as the Morozov discrepancy principle (Scherzer 1993; Pereverzev & Schock 2000) or the L-curve criterion (Miller 1970; Lawson & Hanson 1995), in order to balance errors due to the noise level in the data and the effect of the regularization. The second term, which corresponds to adding a mass matrix term (L^2-type Tikhonov), is needed to make the regularization invertible for the inexact Newton-CG algorithm to converge, since Neunmann boundary conditions are typically imposed on the $\boldsymbol{m}$ field. Here, δ_{L^2} is a scalar parameter that controls the strength of the L^2-type regularization and is much smaller than γ_{H^1}. First and second variations of $\mathcal{R}^{H^1}(\boldsymbol{m})$ in eqs. (7) and (9) are straightforward to derive, since $\mathcal{R}^{H^1}(\boldsymbol{m})$ is explicit in $\boldsymbol{m}$.

A limitation of this Tikhonov-type regularization is that, by design, it smooths out sharp edges of the model parameter field $\boldsymbol{m}$ that may exist at least in parts of the domain. A better approach if sharp contrasts are expected, common in image denoising for example, is to use total variation (TV) regularization (e.g., Rudin et al. 1992; Strong & Chan 2003; Chan et al. 2005), which takes the $L^1(\Omega)$

norm of the gradient rather than the L^2,

$$\mathcal{R}^{TV}(\boldsymbol{m}) = \gamma_{TV} \int_\Omega (\nabla \boldsymbol{m} \cdot \nabla \boldsymbol{m} + \varepsilon)^{\frac{1}{2}} \, \mathrm{d}\boldsymbol{x} + \frac{\delta_{L^2}}{2} \int_\Omega \boldsymbol{m} \cdot \boldsymbol{m} \, \mathrm{d}\boldsymbol{x}, \tag{13}$$

where γ_{TV} controls the strength of the regularization term, and the small positive parameter ε is included to preserve the differentiability of $\mathcal{R}^{TV}(\boldsymbol{m})$ when $\nabla \boldsymbol{m} = \boldsymbol{0}$. Intuitively, TV can be seen to preserve sharp edges as follows. At an interface, $\nabla \boldsymbol{m}$ is unbounded, and squaring it as in Tikhonov H^1 regularization leads to an unbounded integral, which mean the optimizer will avoid such an infinite penalty be smoothing the interface. On the other hand, the square root in TV restores integrability, leading to a finite penalty (in fact equal to the jump in $\boldsymbol{m}$ multiplied by the length of the interface, for a piece-wise homogeneous medium). Thus, if the data are indicative of an interface, TV will seek to preserve it. The first variation of $\mathcal{R}^{TV}$ in eq. (7) reads:

$$\mathcal{R}^{TV}_m(\boldsymbol{m}, \tilde{\boldsymbol{m}}) = \gamma_{TV} \int_\Omega \frac{1}{(\nabla \boldsymbol{m} \cdot \nabla \boldsymbol{m} + \varepsilon)^{\frac{1}{2}}} \nabla \boldsymbol{m} \cdot \nabla \tilde{\boldsymbol{m}} \, \mathrm{d}\boldsymbol{x} + \delta_{L^2} \int_\Omega \boldsymbol{m} \cdot \tilde{\boldsymbol{m}} \, \mathrm{d}\boldsymbol{x}, \tag{14}$$

while the second variation is:

$$\mathcal{R}^{TV}_{mm}(\boldsymbol{m}, \tilde{\boldsymbol{m}}, \hat{\boldsymbol{m}}) = \gamma_{TV} \int_\Omega \frac{1}{(\nabla \boldsymbol{m} \cdot \nabla \boldsymbol{m} + \varepsilon)^{\frac{1}{2}}} \left(I - \frac{\nabla \boldsymbol{m} \otimes \nabla \boldsymbol{m}}{\nabla \boldsymbol{m} \cdot \nabla \boldsymbol{m} + \varepsilon} \nabla \tilde{\boldsymbol{m}} \right) \cdot \nabla \hat{\boldsymbol{m}} \, \mathrm{d}\boldsymbol{x} \tag{15}$$

$$+ \delta_{L^2} \int_\Omega \tilde{\boldsymbol{m}} \cdot \hat{\boldsymbol{m}} \, \mathrm{d}\boldsymbol{x}, \tag{16}$$

where $\otimes$ is the outer product. The highly nonlinear term $\left(I - \frac{\nabla \boldsymbol{m} \otimes \nabla \boldsymbol{m}}{\nabla \boldsymbol{m} \cdot \nabla \boldsymbol{m} + \varepsilon}\right)$ slows the convergence of Newton's method, since the radius of the region of quadratic convergence shrinks as ε decreases and $|\nabla \boldsymbol{m}|$ increases. For this reason in the following, we will replace the second variation of $\mathcal{R}^{TV}$ with the so-called lagged diffusivity variational form:

$$\tilde{\mathcal{R}}^{TV}_{mm}(\boldsymbol{m}, \tilde{\boldsymbol{m}}, \hat{\boldsymbol{m}}) = \gamma_{TV} \int_\Omega \frac{1}{(\nabla \boldsymbol{m} \cdot \nabla \boldsymbol{m} + \varepsilon)^{\frac{1}{2}}} \nabla \tilde{\boldsymbol{m}} \cdot \nabla \hat{\boldsymbol{m}} \, \mathrm{d}\boldsymbol{x} + \delta_{L^2} \int_\Omega \tilde{\boldsymbol{m}} \cdot \hat{\boldsymbol{m}} \, \mathrm{d}\boldsymbol{x}. \tag{17}$$

The resulting method exhibits a first-order convergence rate but becomes more robust for small values of ε and larger $\nabla \boldsymbol{m}$. It is straightforward to show that if ε is large, the total variation behaves like the H^1-type Tikhonov regularization.

3.2 Model setup

To demonstrate the potential of our computational framework in solving heterogeneous media non-linear inverse problems, we consider a 2-D synthetic model inspired by a subduction zone setting. We also want to compare the performance of the two different types of regularization, $\mathcal{R}(\boldsymbol{m})$, namely H^1-type Tikhonov and total variation (TV), to recover the heterogeneous Poisson's ratio structure, $\nu(\boldsymbol{m})$.

The model consists of a curved fault internal boundary and 20 observations of displacements, both

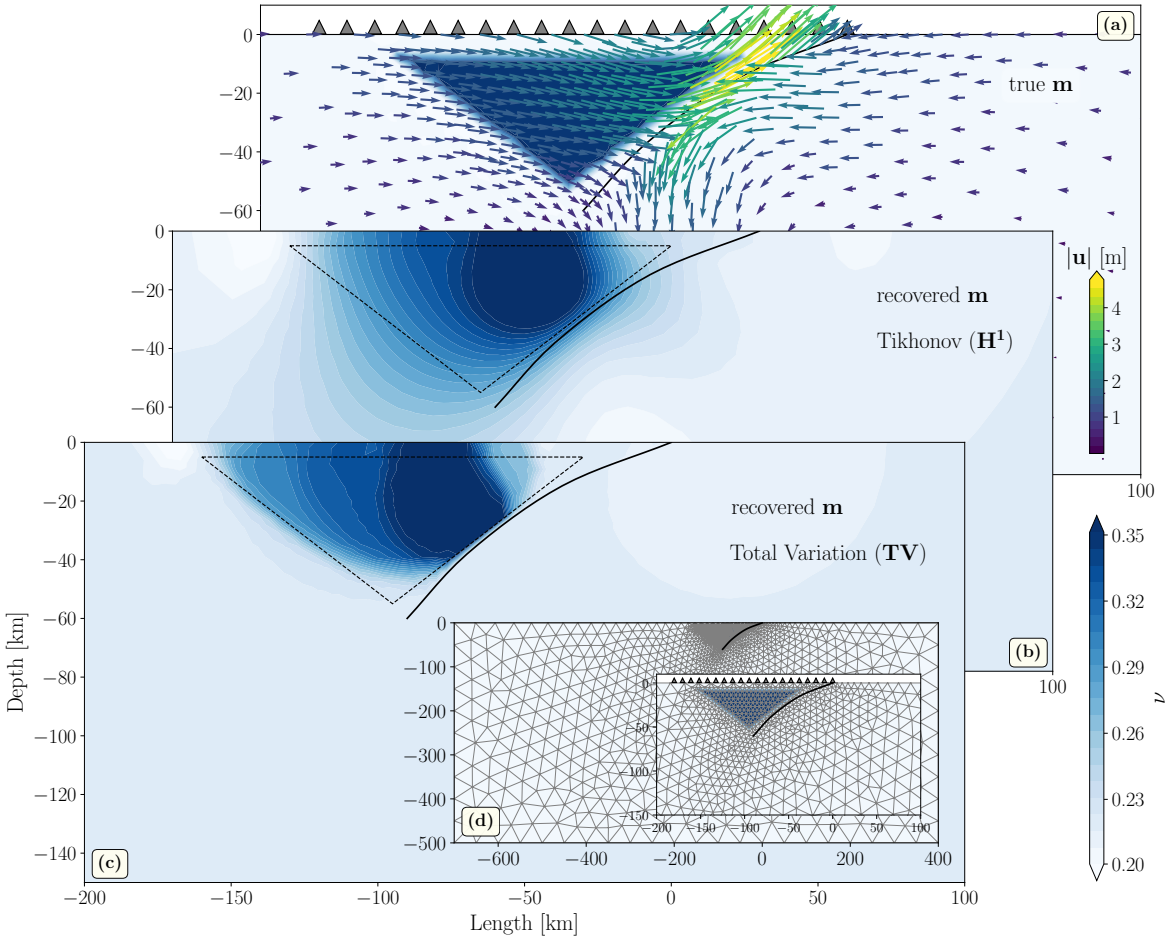

Figure 1. Comparison of the recovered Poisson's ratio, ν, structure between the Tikhonov (b) and total variation (c) regularization. (a) True Poisson's ratio structure (background: $\nu = 0.2$) including the triangular anomaly ($\nu = 0.35$) in the overriding plate. The earthquake displacement is used to compute the 20 synthetic noisy ($\sigma_{\mathrm{d}} = 0.2$ cm) surface displacement data (grey triangles). (d) Finite-element mesh with a zoomed-in view of the mesh refinement around the fault. For comparison, the triangular black dashed line indicates the shape of the material anomaly.

horizontal and vertical, uniformly spaced at the surface in the overriding plate (gray triangles, inset in Fig. 1d, and panel a). We selected this particular network configuration as it resembles the locations of geodetic stations that might monitor subduction zones. The estimated material property field, as well as the associated model uncertainty, are of course highly dependent on the observational sites. The development of scalable approaches for the solution of the associated optimal experimental design problem of determining optimal observation locations is an active area of research (e.g., Alexanderian et al. 2016; Attia et al. 2018; Koval et al. 2020; Wu et al. 2023) and is beyond the scope of this manuscript. The 1,100 $\times$ 500 km rectangular domain contains a triangular Poisson's ratio anomaly of $\nu = 0.35$ located in the overriding plate. This anomaly may resemble, for example, the presence

of fluids or partial melt in the mantle wedge. The background Poisson's ratio is chosen to be $\nu = 0.20$ indicating a more compressible material. The unstructured mesh, generated by the open-source software GMSH (Geuzaine & Remacle 2009), contains 2,391 triangular cells. The mesh is finer close to the fault discontinuity and coarser near the lateral and bottom boundaries (Fig. 1d).

The forward mixed elasticity problem (eq. 3) is discretized using the 1st-order stable triplet of finite-element spaces, resulting in 21,717 degrees-of-freedom (DOFs) for the primary variables (stress, displacement, and rotation). The stress field $\boldsymbol{\sigma}$ is approximated with Brezzi-Douglas-Marini elements (14,544 DOFs). The displacement and rotations vector fields, $\boldsymbol{u}$ and $\boldsymbol{r}$, are approximated by using piece-wise constant discontinuous Galerkin elements, resulting in 4,782 and 2,391 DOFs, respectively. We choose to discretize the Poisson's ratio scalar field $\boldsymbol{m}$ with linear Lagrange elements (1,246 DOFs). Zero displacement boundary conditions are applied to the left, right and bottom boundaries, and a free surface to the top of the model. We assume no body forces and a homogeneous shear modulus of a nominal 30 GPa, where inversions cannot constrain absolute values since we have no stress constraints.

To model an earthquake-like signal, we kinematically prescribe a Gaussian slip distribution on the fault interface. Given the nature of the problem, we are sensitive only to relative displacements with a scale set by the amplitude of fault slip. Thus, only Poisson ratio and shear modulus variations with respect to a reference modulus can be inferred, and not absolute values. However, we use dimensional values with 10 m for peak slip and Earth-like length dimensions to make actual numbers comparable to megathrust cases. The Gaussian slip distribution has the peak slip centered at a depth of 20 km and a standard deviation of 15 km (Fig. 1a). We adhere to the convention where negative slip is associated with thrust faults and positive slip is associated with normal faults. We generate synthetic surface horizontal and vertical displacements recorded at the 20 surface geodetic stations by solving the forward mixed elasticity problem (Fig. 1a). We add Gaussian noise $\mathcal{N}(0, \sigma_{\mathrm{d}}^2)$ to these data, with a mean of zero and a standard deviation of $\sigma_{\mathrm{d}} = 0.2$ cm. This standard deviation value is an average estimate derived from realistic data noise observed at onshore geodetic stations in Japan (e.g., Hatanaka 2005; Iinuma et al. 2012). All computations were performed using a single core of a standard laptop (Intel I9-9880H machine running at 2.4 GHz with 32 GB of RAM).

To analyze the quality of the inverse solution $\boldsymbol{m}$, we can assess the amount of information that can be recovered from the data. We determine the eigenvalues and eigenfunctions of the second derivative of the cost functional $\mathcal{J}(\boldsymbol{m})$ (eq. 4), the Hessian $\mathcal{H}(\boldsymbol{m})$, focusing on its data misfit part. After discretization, the Hessian is generally a large, dense matrix; therefore, an explicit construction of $\mathbf{H}$ for large-scale problems is typically intractable (e.g,. Bui-Thanh & Ghattas 2013; Petra et al. 2014). Each column of the Hessian requires the solution of a pair of linearized forward/adjoint PDEs. The Hessian $\mathbf{H}$ can be decomposed into the Hessian of the data misfit $\mathbf{H}^{\mathrm{misfit}} = \mathbf{J}^T \Gamma_{\mathrm{noise}}^{-1} \mathbf{J} + \sum_i \partial_{mm} [\mathbf{F}]_i \, [\mathbf{F}(\mathbf{m}) -$

$\mathbf{d}]_i$ and the Hessian of the regularization term $\mathbf{H}^{\text{reg}}$. $\mathbf{J}$ is the Jacobian of the discretized parameter-to-observable map $\mathbf{F}(\mathbf{m})$ evaluated at any point, $\mathbf{\Gamma}_{\text{noise}}^{-1} = \frac{1}{\sigma_{\text{d}}^2}\mathbf{I}$ represents the data noise covariance matrix, and $[\cdot]_i$ is the i-th component of the vector. Although the explicit construction of $\mathbf{H}^{\text{misfit}}$ is often intractable, we can leverage the fact that its eigenvalues typically collapse rapidly to zero. Hence, it is possible to build a low-rank spectral decomposition of the misfit part of the Hessian (Ghattas & Willcox 2021). In HIPPYLIB, we employ randomized eigensolvers (Halko et al. 2011) to estimate the eigenvalues λ_i and eigenvectors $\mathbf{v}_i$ of the Hessian misfit by solving the generalized eigenproblem (Villa et al. 2021):

$$\mathbf{H}^{\text{misfit}}\mathbf{v}_i = \lambda_i \mathbf{R}\mathbf{v}_i \qquad \lambda_1 \geq \lambda_2 \geq \cdots \geq \lambda_n, \tag{18}$$

where $\mathbf{R}$ is the discretized regularization operator $\mathcal{R}$, and n is the number of discretized model parameters. Eigenvalues λ_i greater than unity correspond to eigenvectors that can be inferred from the data, while $\lambda_i < 1$ are associated with eigenvectors that are largely influenced by the noise (Villa et al. 2021) and those modes of $\boldsymbol{m}$ cannot be reliably recovered by the inversion.

To quantitatively compare the solutions of the inverse problem we use a metric based on the data information content of the Hessian misfit. We call this metric LDPDH, which is the log-determinant of the preconditioned data misfit Hessian, and it reads:

$$\text{LDPDH} = \frac{1}{2}\log\det(\mathbf{I} + \tilde{\mathbf{H}}^{\text{misfit}}) \approx \frac{1}{2}\sum_{j=1}^{N_\lambda} \ln(1+\lambda_j), \tag{19}$$

where $\mathbf{I}$ is the identity matrix, $\tilde{\mathbf{H}}^{\text{misfit}} = \mathbf{R}^{-\frac{1}{2}}\,\mathbf{H}^{\text{misfit}}\,\mathbf{R}^{-\frac{1}{2}}$ is the regularization preconditioned data misfit Hessian, and λ_j are the eigenvalues of $\tilde{\mathbf{H}}^{\text{misfit}}$ from eq. (18). N_λ is the number of eigenvalues above 1. The greater the LDPDH, the higher is the information content that can be retrieved from the data about the model parameter. In Bayesian optimal experimental design problems, this metric reduces to the expected information gain in the linear inverse problem case (D-optimality criterion) (e.g., Alexanderian et al. 2016). In that context, maximizing the LDPDH with respect to the station's location is equivalent to finding the sensor configuration that maximizes information gain from the data. This metric is independent of the true solution.

3.3 Inversion results with different regularization

After perturbing the synthetic surface displacements with random Gaussian noise, we invert them for the heterogeneous Poisson's ratio spatial distribution using the H^1-type Tikhonov (Fig. 1b) and TV regularization (Fig. 1c), respectively. The Poisson's ratio anomaly is well recovered in both cases, with the highest accuracy at the center of the anomaly. In particular, the Tikhonov regularization blurs the sharp triangular edges, which are better preserved using the TV regularization.

Nevertheless, there is a notable difference in the computational performance of the two inversions. The inversion with the Tikhonov regularization requires 11 iterations to reduce the Ł$_2$ norm of the gradient by 9 orders of magnitude, using penalty weights of $\gamma_{H^1} = 10^2$ and $\delta_{L^2} = 10^{-3}$. On the other hand, the inverse problem with TV regularization exhibits slower convergence, as expected, necessitating 39 iterations with penalty weights of $\gamma_{TV} = 0.5$, $\varepsilon = 10^{-7}$, and $\delta_{L^2} = 10^{-3}$. The slower convergence of the total variation may be attributed to the non-linear term in the denominator of eqs. (14) and (15), and the use of an approximated Hessian.

In our synthetic case, we arbitrarily choose a material anomaly with higher Poisson's ratio than the background. This choice, as well the selected model setup, significantly influences the variations in surface deformation recorded by the observations such as GNSS and InSAR. In the next section, we will investigate the effects of varying the material properties (Poisson's ratio and shear modulus), and the model setup (fault dip) on the surface horizontal and vertical displacements. The differences in displacements caused by the relative contribution between the earthquake source and the heterogeneous medium will also be important in section 4, where we will perform a joint inversion for both fault slip and subduction zone structure.

3.4 Signature of material heterogeneity and fault dip on surface deformation

Why does the inversion for material parameters work, and what sensitivities should we expect in general? While these questions are accessible with formal inverse approaches, it helps to build some intuition as to which of these heterogeneities can be inferred through inversion. To analyze the impact of heterogeneity and fault dip on the recorded surface displacements, we solve the forward problem described in eq. (3). We vary the fault dip angle as well as the values of Poisson's ratio, ν, and shear modulus, μ, within the triangular anomaly relative to the background homogeneous structure ($\nu = 0.20$, $\mu = 30$ GPa). To study the role of fault dip more effectively, we consider a straight fault with a fixed length but varying dip angles of $30°$, $45°$, and $60°$, respectively, instead of a more curved fault geometry (see Fig. 2a).

Fig. 2 illustrates the horizontal and vertical surface displacements as a function of fault dip and triangular material anomaly (shaded in light brown). In subplots (b,c,d,e), the light brown vertical line indicates the location of the trench. The shaded gray areas in panels (b) and (c) indicate the variations of horizontal (b) and vertical (c) displacements assuming a fault dipping at $30°$ (dotted gray line) and $60°$ (solid) to the left, respectively. The orange and blue shaded regions in Fig. 2b,c correspond to changes in surface horizontal and vertical deformation caused by uniformly varying the values of shear modulus and Poisson's ratio in the triangular anomaly, respectively. Specifically, the dashed orange line in panels (d) and (e) represents a shear modulus of 15 GPa, while the solid line represents

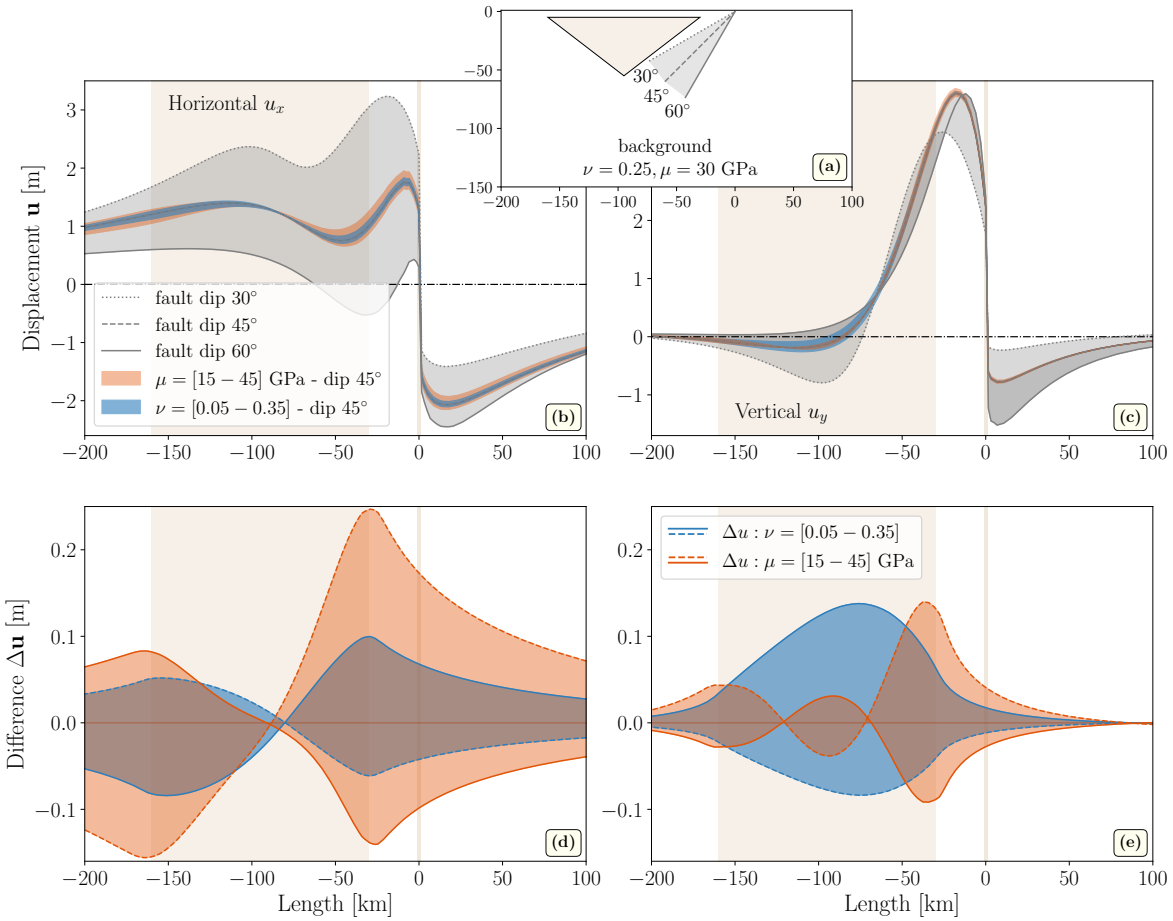

Figure 2. Effect of fault dip and material heterogeneity variations on horizontal and vertical surface displacements. (a) Reference model configuration with the triangular material anomaly (shaded light brown) and straight faults with different fault dips. (b) and (c) demonstrate the changes in horizontal and vertical surface deformations, respectively, by varying the fault dip (grey shaded area), shear modulus (orange area), and Poisson's ratio (blue area). The shaded brown area delineates the region of the material anomaly, while the line indicates the location of the trench. (d) and (e) a zoomed-in view of panels (b) and (c) representing the differences in horizontal (d) and vertical (e) displacements when varying the shear modulus μ (orange) and Poisson's ratio ν (blue), considering a fault dipping at an angle of $45°$, in comparison to a homogeneous background structure.

45 GPa. For the Poisson's ratio, the solid blue line represents 0.05, and the dashed line represents 0.35. Panels (d) and (e) show a zoomed-in view of the differences in surface horizontal and vertical displacements resulting from variations in μ and ν within the triangular anomaly, compared to the homogeneous case ($\nu = 0.20$, $\mu = 30$ GPa) for a fault dipping $45°$.

First, as expected, the changes in surface deformation caused by material heterogeneity are significantly smaller compared to those caused by differences in fault dip. This effect will also influence the results of the joint inversion for both fault slip and subduction zone structure (refer to section 4). Sec-

ond, as has also been discussed, variations in fault dip have a greater impact on the recorded surface deformation, as shown by the gray shaded area in Fig. 2b and (c), which is much more pronounced than changes in material properties. Shallower faults result in more trenchward motion and subsidence in the overriding plate compared to deeper faults. Furthermore, the peak of the uplift is more trenchward for faults with a steeper dip angle than for shallower faults (panel c).

Regarding the changes in material properties within the triangular anomaly, more incompressible materials result in a second region of more trenchward motion in the western part of the anomaly, and a more landward in the eastern portion of it (dashed blue line in Fig. 2d). Conversely, the opposite occurs with a more compressible material anomaly (blue solid line). A similar effect can be seen with a weaker material (represented by the orange dashed line), although the variations in magnitude are higher, suggesting that changes in μ primarily affect the horizontal components of the surface displacement field. On the other hand, the vertical component (Fig. 2d) is more influenced by variations in Poisson's ratio rather than the shear modulus (blue shaded area). Materials with higher Poisson's ratios lead to more subsidence compared to a homogeneous structure (represented by the blue dashed line), while lower ν result in more uplift (blue solid line). The highest uplift/subsidence occurs in the middle of the anomaly, where the anomaly has a greater vertical extent.

The behavior of the heterogeneous shear modulus is more complex than that of the Poisson's ratio. In the case of a weaker material within the triangular anomaly, there is greater subsidence in the central part of the anomaly and increased uplift at the sides (as shown by the orange dashed line in Fig. 2d) compared to the homogeneous case. Conversely, for stronger μ anomalies, the resulting surface vertical displacement exhibits more uplift at the center and more subsidence at the sides of the anomaly. Furthermore, we observe that the influence of material heterogeneity on surface deformation extends beyond the lateral extent of the anomaly. It also affects the far field, particularly in the horizontal component (Fig. 2d).

3.5 Role of noise and number of observations in the inverse solution

While the forward tests show that heterogeneity effects can be subtle, we nonetheless found that our framework can satisfactorily invert for Poisson's ratios for certain geometries. Using the TV regularization, we now further investigate the parameters that affect resolution.

To quantify the impact of noise on the eigenvalues and the inverse solution, we examine how the metric LDPDH (log-determinant of the preconditioned data misfit Hessian) decreases with increasing noise levels in the deformation data. The regularization parameters are kept fixed and equal to the test above (Fig. 1). Fig. 3 illustrates the relationship between the LDPDH (eq. 19) and the noise level in the surface data. The x-axis represents the noise level percentage, calculated by normalizing the

standard deviation of the noise with the L_∞ norm of the surface displacements. It is evident that the LDPDH decreases non-linearly as the data become noisier. Panels (A-F) present six examples of the inferred spatial field of Poisson's ratio obtained through inversion by varying the noise level. We keep the number of evenly-spaced surface stations fixed at 20 (gray triangles) and the earthquake source depth at 20 km. We note that with noise-free data, the triangular shape of Poisson's ratio anomaly can be nearly fully reconstructed (Panel A), with imperfection likely due to the small number of surface observations (20); internal constraints such as from seismological or electro-magnetic imaging could be implemented as well.

Increasing the noise level in the data gradually reduces the resolution of the inverse solution at the edges of the anomaly. As the noise increases, the difference between the background and the

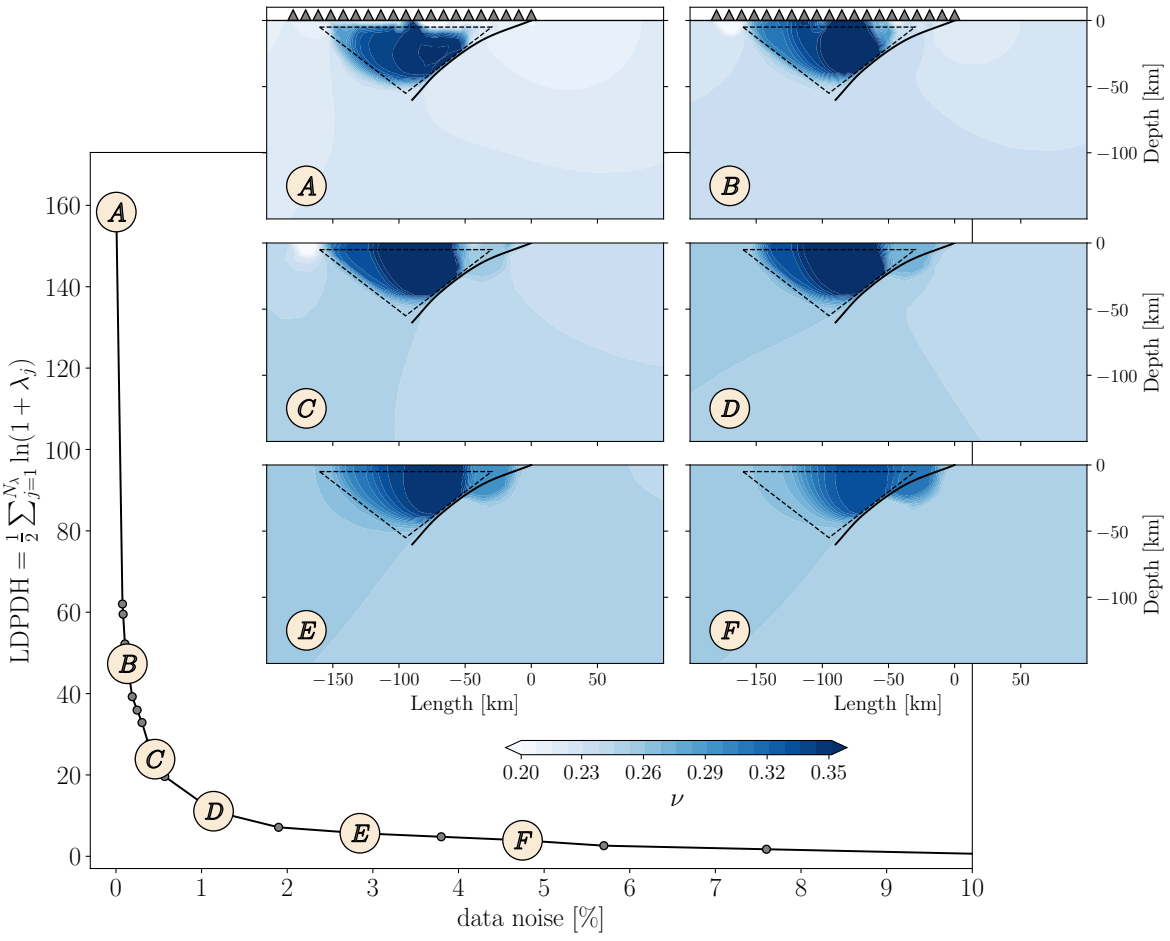

Figure 3. Role of noise level in the inverse solution of Poisson's ratio. The metric LDPDH is measured as a function of data noise percentage. Examples (A), (B), (C), (D), (E), and (F) illustrate the inferred value of ν (Poisson's ratio) for various noise levels, based on 20 surface observations (showed as grey triangles in panels A and B). For comparison, the triangular black dashed line indicates the shape of the material anomaly.

anomaly diminishes. However, it is still possible to detect the geometry of the anomaly (panels B to D). Typically, realistic values of data noise for onshore horizontal and vertical GNSS stations range from $\sigma_{\mathrm{d}} = 0.2 - 1.5$ cm, respectively (e.g. Hatanaka 2005). In our model, this corresponds to noise percentages of about $0.08 - 0.6\%$ (panels B and C). When the noise exceeds 3%, a reliable recovery of the Poisson's ratio anomaly becomes challenging (panel F), as might be expected, and additional constraints, e.g., on the geometry of likely anomalies, would be needed.

In addition to the noise level in the data, there are other factors that affect the resolution of the inverse solution. One such factor is the number of surface observations. Intuitively, having more surface stations available should provide more information gained from the data about the Poisson's ratio structure. To verify this hypothesis and quantify the contribution of the number of stations, we can vary the number of surface observations while keeping the data noise level fixed at $\sigma_{\mathrm{d}} = 0.2$ cm, and maintaining the same setup as before—i.e. earthquake depth equal to 20 km depth and same regularization weights as above. Fig. 4 illustrates the LDPDH (eq. 19) as a function of the number of surface sensors, assuming evenly-spaced stations located in the overriding plate and within the same length range as the previous tests. These results will differ if the stations were optimally distributed rather than evenly spaced. However, determining the optimal station configuration would require solving a Bayesian optimal experimental design (OED) problem which we do not attempt here.

Panels (A-F) represent six examples of the recovery of the Poisson's ratio triangular anomaly from the non-linear inversion by varying the number of surface geodetic stations. Higher LDPDH values indicate a more reliable inference of additional eigenmodes from the data. The LDPDH rapidly increases from nearly zero to approximately 75 as the number of stations increases from 1 to $20 - 25$, as shown in panels (A), (B), and (C), as might be expected. However, adding more than 25 surface stations does not lead to a significant improvement in the inverse solution. Panels (D), (E), and (F) clearly demonstrate that a higher number of surface geodetic sensors does not necessarily result in a better recovery of the material anomaly. The logarithmic-type saturation in the metric vs. station number curve indicates diminishing returns of adding more stations given the station-anomaly configuration indicating redundancy.

Figure 5 summarizes these results along with an analysis of the role of earthquake source depth. To perform these tests, we employ the same model setup as Fig. 1, including the fault geometry and mesh discretization. In panel (a) representing the spectrum decay, we consider an earthquake originating at a depth of 20 km with 20 evenly-spaced surface observations, and we vary the noise level of the surface displacement data (Fig. 3). In panel (b), where we analyze the number of observations, we set the data noise level to $\sigma_{\mathrm{d}} = 0.2$ cm and maintain the earthquake depth at 20 km. Regarding the earthquake source depth, we assume a data noise level of $\sigma_{\mathrm{d}} = 0.2$ cm and use 20 evenly-spaced

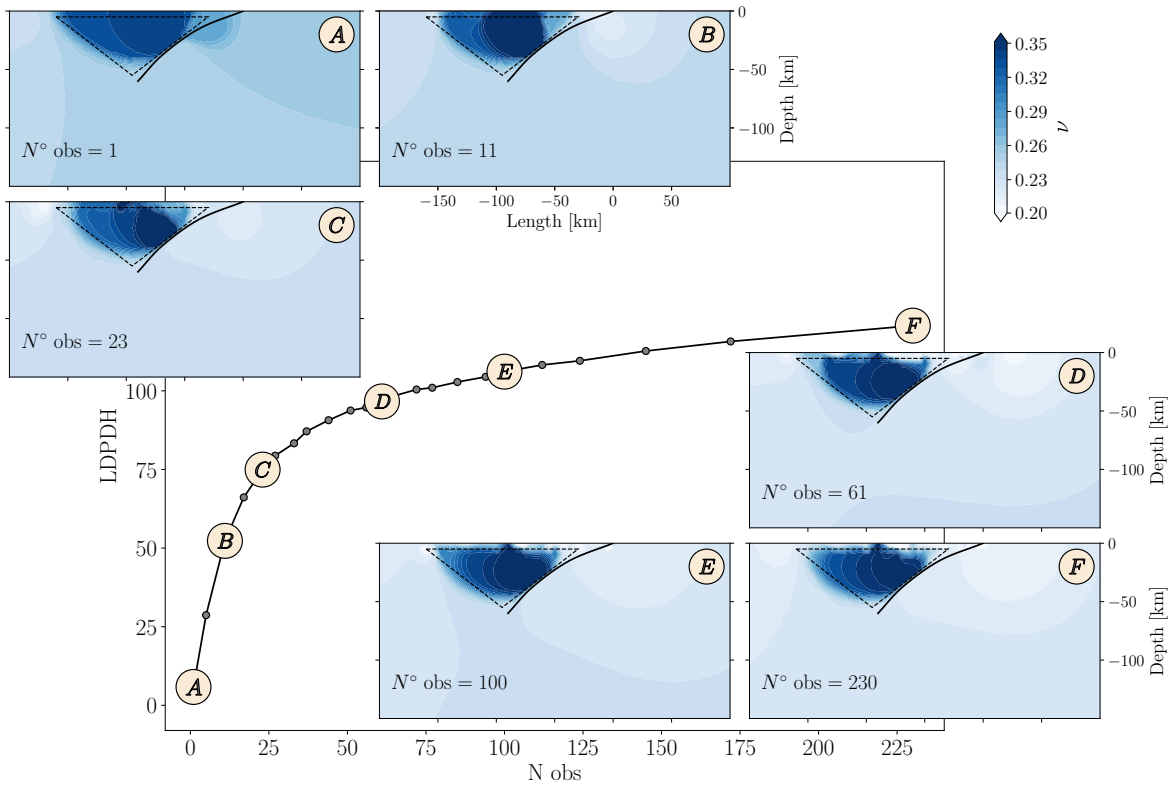

Figure 4. Role of the number of surface stations in the inverse solution for Poisson's ratio. The metric LDPDH is examined as a function of the number of observations. Examples (A-F) represent inferred values of ν for different numbers of sensors, assuming a noise level of 0.2 cm. For comparison, the triangular black dashed line indicates the shape of the material anomaly.

surface observations. We plot the eigenvalue decay of the regularization-preconditioned data misfit Hessian, $\tilde{\mathbf{H}}^{\text{misfit}}$ (eq. 18), as a function of data noise (a), the number of surface observations (b), and earthquake depth (c). Darker colors represent low noise, a large number of sensors, and shallower earthquakes, respectively. The gray dotted line at $\lambda = 1$ in all three subplots represents the threshold above which the eigenmodes associated with the corresponding eigenvalues are predominantly determined by the data (Villa et al. 2021). Eigenmodes corresponding to generalized eigenvalues below unity are strongly penalized by the regularization. In the inset plots, we show the LDPDH as a function of the three parameters.

By comparing the spread of the Hessian data misfit spectrum with respect to the three different parameters, it becomes evident that data noise plays the most significant role in influencing the recovery of the material anomaly. In fact, by changing the noise level from zero to about 10 per cent, the eigenvalues spread several orders of magnitude (panel a). As expected, the second most influential factor affecting the quality of the inverse solution is the number of surface observations (Fig. 5b),

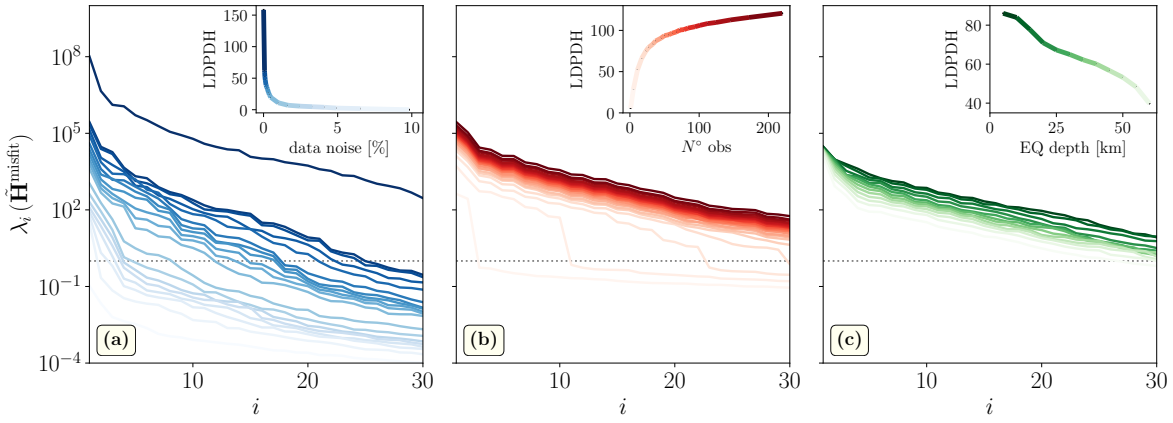

Figure 5. Eigenvalue decay of the regularization-preconditioned data misfit Hessian, $\tilde{\mathbf{H}}^{\text{misfit}}$ (eq. 18) and LDPDH (insets) as a function of data noise (a), number of surface observations (b), and earthquake depth (c), respectively.

followed by the earthquake depth (c). Regarding the latter, it is evident that shallower earthquakes provide more valuable information about the inverse solution (refer to the inset in panel c). In fact, the eigenvalue spread decreases almost linearly as the depth of the earthquake source increases. This observation is logical since surface displacements caused by shallower depths are larger and contain more information about the structure of the subduction zone.

So far, we have considered a known fault source, which might, in reality, be inferred from a given fault geometry and constraints other than geodesy on slip, e.g. from radiated seismic waves. However, more commonly, we do not know the slip distribution, and it is important to quantify trade-offs between structure and slip. We thus proceed to discuss inversions where fault slip is solved for simultaneously with material heterogeneity.

4 JOINT INVERSION FOR HETEROGENEOUS STRUCTURE AND FAULT SLIP

We build upon the non-linear inversion method described in section 3, as well as the coseismic slip inversion of Puel et al. (2022). Below, we outline the formulation of the gradient and Hessian action expressions for the deterministic joint inversion at the infinite-dimensional level—i.e., the continuous integral level—similar to section 3. Subsequently, we provide an example of the inverse result using a 2-D synthetic test and investigate the trade-off between inferring fault slip and the structure of shear modulus.

4.1 Infinite-dimensional deterministic joint inverse formulation

Our objective is to simultaneously invert surface geodetic data for both fault slip and structure, for which we now choose shear modulus as the parameter of interest for comparison with previous forward studies (e.g., Williams & Wallace 2015, 2018; Hashima et al. 2016). We consider an infinite-dimensional Hilbert space of functions $\mathcal{M} = \mathcal{M}_s \times \mathcal{M}_\mu$ defined in the domain Ω, and sparse noisy finite-dimensional surface displacement geodetic data $\mathbf{d} \in \mathbb{R}^{n_{\text{obs}}}$. Our goal is to find the optimal fault slip distribution $\boldsymbol{m}_s \in \mathcal{M}_s$ and shear modulus spatial field $\mu(\boldsymbol{m}_\mu)$, with $\boldsymbol{m}_\mu \in \mathcal{M}_\mu$, that predict the surface deformation caused by earthquakes. Similar to the inversion for Poisson's ratio, we choose to invert for the argument of the hyperbolic tangent to constrain the shear modulus, such that $\mu(\mathbf{m}_\mu) = \mu_0[1 + \tanh(\mathbf{m}_\mu)]$. This constraint ensures that the shear modulus remains within a specified range of values. Here, μ_0 represents the mean of the chosen range, for example, 30 GPa, recalling that we are only sensitive to relative variations of μ with respect to some scaling μ_r rather than absolute values. For our example, the allowable range for the shear modulus variation is between zero and $2\mu_0$. This choice of constraining the shear modulus within a range improves the well-posedness of the joint inverse problem. Furthermore, this choice is often realistic as we may have prior knowledge of the expected range of μ. The detailed expression for $\mu(\mathbf{m}_\mu)$ does not significantly impact the results (see section 4.4).

To derive the gradient and Hessian expressions for this inverse problem, we employ an analogous approach as described in section 3. However, in this case, we introduce two model parameters, $\boldsymbol{m}_\mu$ and $\boldsymbol{m}_s$, instead of just one. By utilizing the Lagrangian formalism (Tröltzsch 2010), we can derive the adjoint problem, which is similar to the Poisson's ratio problem, with the exception of the first term. In this term, we substitute $\mathbf{m}_\mu$ instead of μ in the elastic compliance expression (Eq. 2). By taking the derivative of the Lagrangian functional of the gradient with respect to the model parameters $(\boldsymbol{m}_\mu, \boldsymbol{m}_s)$, we obtain the pointwise gradient expression in a arbitrary direction $(\tilde{\boldsymbol{m}}_\mu, \tilde{\boldsymbol{m}}_s)$:

$$
\begin{aligned}
\big(\mathcal{G}(\boldsymbol{m}_\mu, \boldsymbol{m}_s), (\tilde{\boldsymbol{m}}_\mu, \tilde{\boldsymbol{m}}_s)\big) &= (\mathcal{R}_{m_\mu}(\boldsymbol{m}_\mu), \tilde{\boldsymbol{m}}_\mu) + (\mathcal{R}_{m_s}(\boldsymbol{m}_s), \tilde{\boldsymbol{m}}_s) \\
&+ \int_\Omega \frac{\mu_m(\boldsymbol{m}_\mu)\tilde{\boldsymbol{m}}_\mu}{2\mu^2(\boldsymbol{m}_\mu)} \left[\boldsymbol{\sigma} - \frac{\nu}{1+\nu(d-2)} \operatorname{tr}(\boldsymbol{\sigma})\boldsymbol{I}\right] : \boldsymbol{\tau}\, \mathrm{d}\boldsymbol{x} \\
&- \int_{\Gamma_F} \tilde{\boldsymbol{m}}_s \cdot \left[T(\mathbf{n}_{\Gamma_F})(\boldsymbol{\tau}\, \mathbf{n}_{\Gamma_F})\right] \mathrm{d}\boldsymbol{S} \qquad \forall (\tilde{\boldsymbol{m}}_\mu, \tilde{\boldsymbol{m}}_s) \in \mathcal{M},
\end{aligned}
\tag{20}
$$

where μ_m is the derivative of $\mu(\boldsymbol{m}_\mu)$ with respect to $\boldsymbol{m}_\mu$, and $\mathcal{R}_{m_\mu}(\boldsymbol{m}_\mu)$ and $\mathcal{R}_{m_s}(\boldsymbol{m}_s)$ are the derivatives of the regularization of the shear modulus and fault slip with respect to $\boldsymbol{m}_\mu$ and $\boldsymbol{m}_s$, respectively. To find the expression of the Hessian action in a direction $(\hat{\boldsymbol{m}}_\mu, \hat{\boldsymbol{m}}_s)$, we need to take the derivative of the second-order Lagrangian functional with respect to the model parameters $(\boldsymbol{m}_\mu, \boldsymbol{m}_s)$

to get:

$$\begin{aligned}\big((\tilde{\boldsymbol{m}}_\mu, \tilde{\boldsymbol{m}}_s), \mathcal{H}(\boldsymbol{m}_\mu, \boldsymbol{m}_s)\,(\hat{\boldsymbol{m}}_\mu, \hat{\boldsymbol{m}}_s)\big) &= (\tilde{\boldsymbol{m}}_\mu, \mathcal{R}_{mm}(\boldsymbol{m}_\mu)\,\hat{\boldsymbol{m}}_\mu) + (\tilde{\boldsymbol{m}}_s, \mathcal{R}_{mm}(\boldsymbol{m}_s)\,\hat{\boldsymbol{m}}_s) \\ &+ \int_\Omega \frac{\mu(\boldsymbol{m}_\mu)\,\mu_{mm}(\boldsymbol{m}_\mu) - \mu_m^2(\boldsymbol{m}_\mu)}{\mu^3(\boldsymbol{m}_\mu)}\,\tilde{\boldsymbol{m}}\hat{\boldsymbol{m}}\,\left[\boldsymbol{\sigma} - \frac{\nu}{1+\nu(d-2)}\,\mathrm{tr}(\boldsymbol{\sigma})\boldsymbol{I}\right] : \boldsymbol{\tau}\,\mathrm{d}\boldsymbol{x} \\ &+ \int_\Omega \frac{\mu_m(\boldsymbol{m}_\mu)\tilde{\boldsymbol{m}}_\mu}{2\mu^2(\boldsymbol{m}_\mu)}\left[\boldsymbol{\sigma} - \frac{\nu}{1+\nu(d-2)}\,\mathrm{tr}(\boldsymbol{\sigma})\boldsymbol{I}\right] : \hat{\boldsymbol{\tau}}\,\mathrm{d}\boldsymbol{x} \\ &+ \int_\Omega \frac{\mu_m(\boldsymbol{m}_\mu)\tilde{\boldsymbol{m}}_\mu}{2\mu^2(\boldsymbol{m}_\mu)}\left[\hat{\boldsymbol{\sigma}} - \frac{\nu}{1+\nu(d-2)}\,\mathrm{tr}(\hat{\boldsymbol{\sigma}})\boldsymbol{I}\right] : \boldsymbol{\tau}\,\mathrm{d}\boldsymbol{x} \\ &- \int_{\Gamma_F} \tilde{\boldsymbol{m}}_s \cdot \left[T(\mathbf{n}_{\Gamma_F})(\hat{\boldsymbol{\tau}}\,\mathbf{n}_{\Gamma_F})\right]\mathrm{d}\boldsymbol{S} \qquad \forall(\tilde{\boldsymbol{m}}_\mu, \tilde{\boldsymbol{m}}_s) \in \mathcal{M},\end{aligned} \tag{21}$$

where μ_m and μ_{mm} denote the first and second derivatives of $\mu(\boldsymbol{m}_\mu)$ with respect to $\boldsymbol{m}_\mu$, respectively. $\boldsymbol{\sigma}$ and $\boldsymbol{\tau}$ are the solutions of the forward and adjoint problems, respectively, and $\hat{\boldsymbol{\sigma}}$ and $\hat{\boldsymbol{\tau}}$ are the solutions of the incremental forward and adjoint problems, respectively (Appendix C). We observe that the expressions for the gradient and Hessian, in this case, are more complex compared to those used for the Poisson's ratio inverse problem (eqs. 7 and 9). This complexity arises from the presence of the shear modulus parameter in the denominator of both the shear and volumetric components in eq. (2). The derivation of the fault slip part is straightforward in both the gradient and Hessian expressions. These expressions can be implemented in HIPPYLIB, although the library only requires the variational form of the forward problem, since it automatically computes first and second derivative information using the symbolic differentiation capabilities of the FENICS library. Once we have the expressions for the gradient and Hessian action, we can apply the inexact Newton-CG algorithm, similar to section 3, to solve the joint inversion.

4.2 Results of joint inversion tests

We consider the same 2-D finite-element mesh as the Poisson's ratio problem (section 3) and test for a triangular anomaly of shear modulus in the overriding plate of 26.5 GPa and the background structure with reference value $\mu_r = 39.5$ GPa, where Earth-like values are used for illustrative purposes but sensitivity is only relative to μ_r, i.e. we are solving for a $\approx$33% reduction in shear modulus (Fig. 6a). We fix the Poisson's ratio to be 0.25 and homogeneous throughout the entire domain. We keep the same 20 surface stations configuration as the Poisson's ratio problem. To discretize the mixed elasticity problem, we use the 2nd-order stable triplet of finite-element spaces, resulting in 57,681 DOFs for the state variables (stress, displacement, and rotation). In this case, the displacement field is approximated with piece-wise linear elements. However, since we are building the 2-D synthetic data with the same order of discretization of the forward problem, the solution should be independent of the discretization order.

We choose to discretize both $\boldsymbol{m}_\mu$ and $\boldsymbol{m}_s$ using continuous piece-wise linear Lagrange elements, resulting in 2,492 DOFs. The surface synthetic data are generated by prescribing the same Gaussian slip as the Poisson's ratio problem, centered at a depth of 20 km with a standard deviation of 15 km and a magnitude of 10 m. The resulting displacement field caused by this model setup is shown in Figure 6a. Then, we perturb these data using the same Gaussian random noise as in section 3 ($\sigma_{\text{d}} = 0.2$ cm) and invert those for both the fault slip $\boldsymbol{m}_s$ and the shear modulus $\mu(\boldsymbol{m}_\mu)$. We use $\mathcal{R}^{H^1}$ (eq. 12) to regularize the fault slip component and the TV regularization (eq. 13) for the shear modulus part to better preserve the sharp edges, similarly to the Poisson's ratio problem. We use $\varepsilon = 10^{-7}$, $\gamma_{TV} = 0.1$, $\gamma_{H^1} = 0.2$, and $\delta_{L^2} = 2 \cdot 10^{-4}$ as penalty terms. The joint inversion converges in 49 Newton iterations.

Figures 6a and (b) show the true variations in the shear modulus used to build the synthetic surface data and the recovered structure from the joint inversion, respectively; we plot the variations of μ by removing its mean such that $\Delta\mu(\boldsymbol{m}_\mu) = \mu(\boldsymbol{m}_\mu) - \bar{\mu}(\boldsymbol{m}_\mu)$, where $\bar{\mu}(\boldsymbol{m}_\mu)$ is the mean solution.

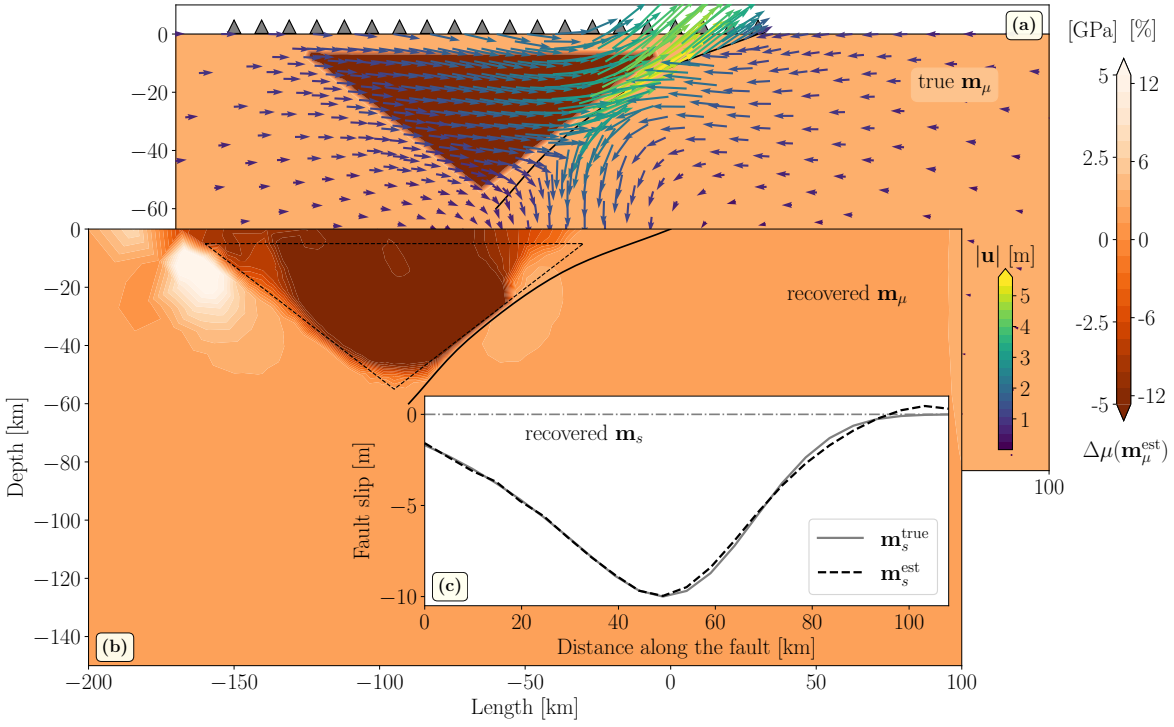

Figure 6. Solution of the joint inverse problem. (a) True variations in the shear modulus structure, $\Delta\mu(\boldsymbol{m}_\mu)$, and earthquake displacements used to compute the 20 synthetic noisy ($\sigma_{\text{d}} = 0.2$ centimeters) surface data (grey triangles). (b) Recovered shear modulus structure variations obtained from the joint inversion in actual units and normalized by the reference μ_r of the background. (c) The inferred fault slip is shown as a black dashed line, compared to the true slip distribution represented by the grey solid line. For comparison, the triangular black dashed line in panel (b) indicates the shape of the material anomaly.

Percentage values indicate the same results with respect to the scaling μ_r. Panel (c) represents the recovered fault slip $\boldsymbol{m}_s$ from the same joint inverse problem. We can see that both the shear modulus structure and the fault slip are well recovered, with some indication of minor spurious oscillation in the shear modulus. However, the overall anomaly is accurately resolved, exhibiting similar variations to the true structure. Using Tikhonov type regularization, rather than TV, we could remove those oscillations to the detriment of inferring anomaly geometries. In Fig. 6b, we observe a loss of resolution in the vertical component of the anomaly due to the surface-only data, and the top-right edge of the triangular anomaly is not well resolved. This limitation may be attributed to the majority of the slip being concentrated in that region (panel a). The surface displacements are primarily influenced by the fault slip rather than the heterogeneous structure (cf. Fig. 2a and b), resulting in a good fit of the inferred slip near the surface (panel c, left), but a poor fit for the shear modulus recovery. In the next section, we will better examine the relative contributions of fault slip and material heterogeneity in the joint inverse problem.

4.3 Trade-off analysis between shear modulus and fault slip

From Fig. 2 we know that the effect of the fault slip on surface displacements is larger than the heterogeneous material structure. Here, we aim to show how various combinations of fault slip and subduction zone structure can produce the same surface displacements. We consider the same 2-D model setup of the joint inverse problem (Fig. 6). We solve the forward problem given a reference earthquake of 10 m of Gaussian coseismic slip, centered at 20 km depth and standard deviation of 15 km depth, and a triangular shear modulus anomaly. As above, we assign $\mu = 26.5$ GPa in the anomaly and $\mu = \mu_r = 39.5$ GPa for the background. We compute the horizontal and vertical surface displacements, denoted as $\mathbf{d}^{\mathrm{ref}}$, for this reference model at the same 20 observations as in Fig. 6a.

Then, we slightly perturb both the magnitude of the fault slip $\boldsymbol{s} + \Delta\boldsymbol{s}$ and the shear modulus triangular anomaly $\mu + \Delta\mu$, while keeping the background structure and earthquake depth fixed. We then recompute the surface displacements $\mathbf{d}$. Lastly, we compare the surface deformation of this perturbed model with that of the reference model by computing the ℓ_2 error: $\|\mathbf{d} - \mathbf{d}^{\mathrm{ref}}\|_{\ell_2} = \sum_{j=1}^{n_{\mathrm{obs}}} (d_j - d_j^{\mathrm{ref}})^2$. We repeat the same procedure by solving approximately 2,500 forward problems, considering constant perturbations of fault slip $|\Delta\boldsymbol{s}|$ between -8 and 8 meters, and $\Delta\mu$ ranging from -26 to 70 GPa. Fig. 7 shows the results of this test. We can interpret this plot as a model space representing the two model parameters, $\boldsymbol{s}$ and μ, and it demonstrates how various combinations of these parameters can yield identical surface displacements. It is apparent that shear modulus variations are less well constrained than the fault slip; i.e., the solution of the joint inversion is not unique, in particular for the heterogeneous medium component, as expected from Fig. 2.

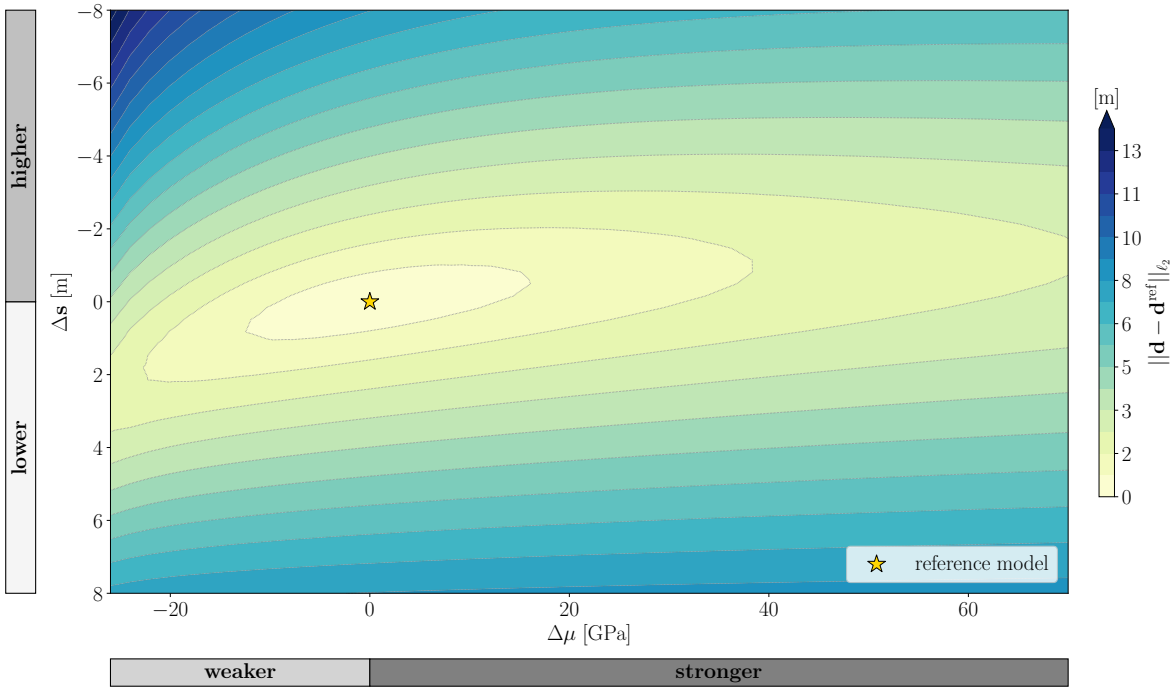

Figure 7. Trade-off between the shear modulus structure and the fault slip contribution in the surface displacements. The contour lines delineate regions with the same ℓ_2 error for surface deformation between the perturbed models and the reference model (represented by a yellow star, where $\Delta \boldsymbol{s} = \Delta\mu = 0$). Lighter colors indicate lower ℓ_2 error, while darker colors represents higher data misfit. The yellow star indicates our reference model, where $\Delta \boldsymbol{s} = \Delta\mu = 0$.

4.4 Effect of shear modulus parameterization in the joint inverse solution

We now proceed to test the effect of how relative shear modulus variations are parameterized. We adopt the same model setup as described in section 4.2. The 2-D synthetic displacements are computed using the same true fault slip as mentioned earlier, and we consider the same 20 surface observations. We use the same TV regularization for the shear modulus component and Tikhonov for the fault slip, respectively, with identical penalty weights as above. After polluting these data with random Gaussian noise $\mathcal{N}(0, 0.2\,\mathrm{cm})$, we perform four joint inversions by varying the range of allowable values for the shear modulus variations. In three of these tests, we invert for the argument of the hyperbolic tangent to determine the shear modulus field, following a similar approach as shown in Fig. 6. For these tests, we utilize a mathematical expression of the form $\mu(\mathbf{m}_\mu) = \frac{\mu_0}{\alpha}[\alpha + \tanh(\mathbf{m}_\mu)]$. Here, μ_0 is set to 33 GPa, and α is chosen as 10, 5, and 2.5 to confine μ within a range that is 0.5, 1, and 2 times the true range, respectively. In the last test, we invert for the argument of the exponential function, i.e. $\mu(\mathbf{m}_\mu) = \exp(\boldsymbol{m}_\mu)$, to ensure the shear modulus remains positive. Our objective is to compare

whether reliable estimates of both fault slip and subduction zone structure can be achieved regardless of the choice of $\mu(\boldsymbol{m}_\mu)$.

Fig. 8 illustrates the inferred fault slip (panel e) and the variations in the shear modulus structure $\Delta\mu(\boldsymbol{m}_\mu)$ (with the mean removed) for these tests. Panels (a) through (c) show the recovered heterogeneous material structure by constraining μ to vary between one half and two times the true range of shear modulus. In panel (d) we slightly modify the $\mu(\boldsymbol{m}_\mu)$ expression to invert for the argument of the exponential. The inferred fault slip and the heterogeneous material structure are quite stable, irrespective of the expressions used for the joint inversion. Specifically, the triangular material anomaly is accurately recovered with a similar shape as shown in Fig. 6. Furthermore, the magnitude of the variations in shear modulus remains consistent, except when the range is only half of the true $\Delta\mu(\boldsymbol{m}_\mu)$, as expected. When the shear modulus is allowed to vary within a wider range the inverse solution is very similar regardless of the mathematical expression used (panels c and d). Overall, the inferred slip is also quite similar in particular at shallow depths (left panel e), and there are only slight differences near the deeper edge of the fault (right panel). This discrepancy is again likely due to geodetic data being limited to the surface, resulting in larger slip uncertainties in the deeper segments of the fault interface. Our analysis focuses only on the deterministic inverse problem. The estimation of the model uncertainties of both parameters associated with this non-linear inversion will require the solution of a Bayesian inverse problem (e.g., Stuart 2010; Bui-Thanh et al. 2013; Beskos et al. 2017), and will be addressed in future research.

4.5 Role of fault dip in the joint inverse solution

In all the tests we have conducted so far, we have relied on the assumption that the fault geometry is known. We now explore the role of uncertainty in fault geometry. To simplify the analysis, we focus on a 2-D synthetic test similar to the one discussed previously. Instead of a curved fault, we consider a dipping straight fault, allowing us to vary only one parameter, the fault dip. We keep the same data noise $\sigma_{\rm d} = 0.2$ cm as the previous tests. As our reference model, we consider a fault dipping at 45° to the left and calculate the 2-D synthetic horizontal and vertical displacements at the same 20 surface observations as in Fig. 6. Then, we perform multiple joint inversions using these data, varying the fault dip angle between 40 and 50°. The results are shown in Fig. 9. Panels (a) through (j) display the recovered heterogeneous shear modulus structure, while panel (k) shows the inferred fault slips by varying the fault dip angle (panel l).

When the synthetic surface data is inverted using the reference model (fault dip equals to 45°), both the fault slip (yellow line in panel k) and the subduction zone structure (panel e) are accurately recovered. Regarding the inferred slip distributions (Fig. 9k), we can see that the slip is under-predicted

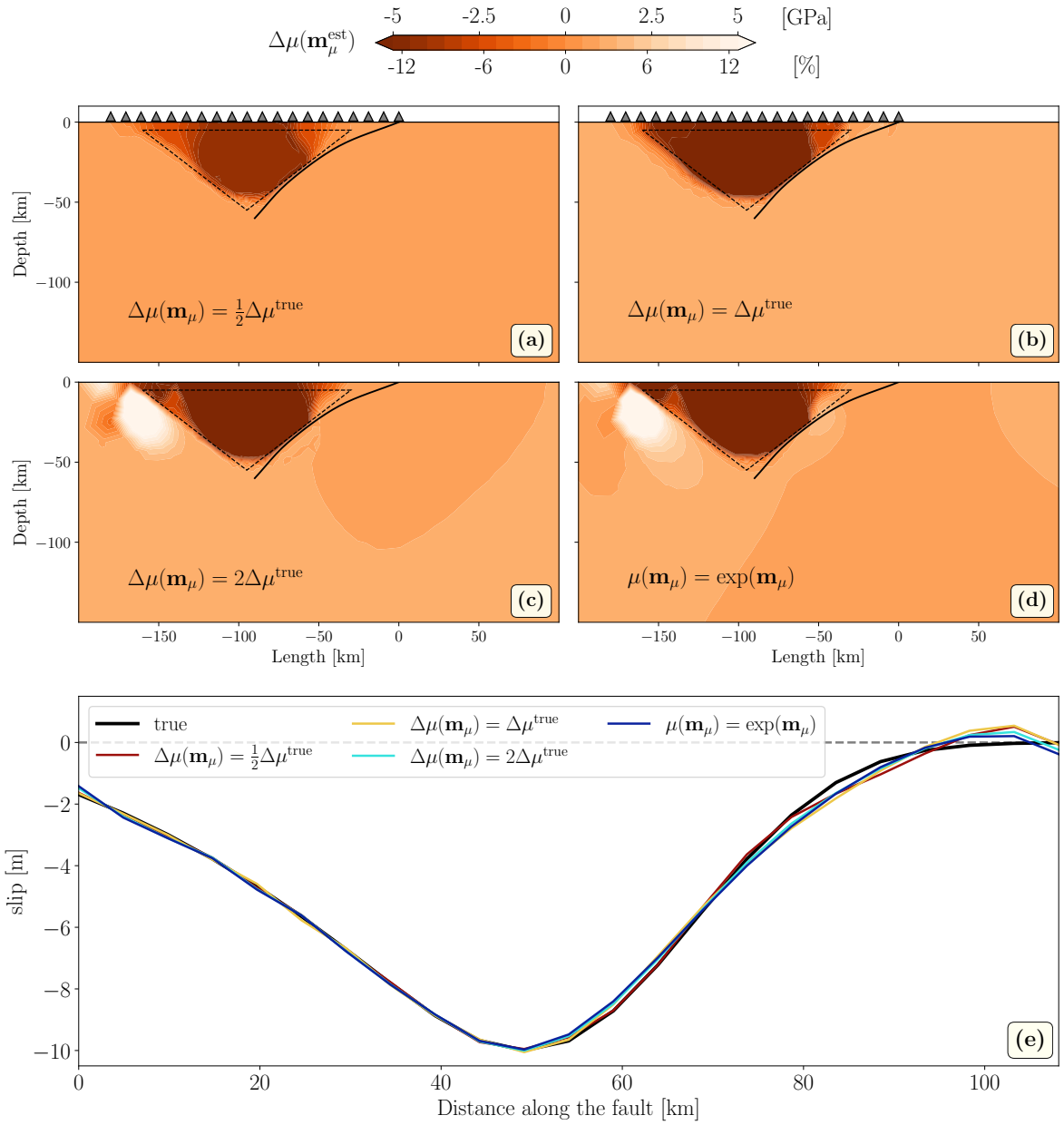

Figure 8. Comparison of fault slip solutions and variations in shear modulus structure from the joint inversion, considering different choices of the mathematical expressions $\mu(\boldsymbol{m}_\mu)$. Panels (a) to (c) illustrate the inferred heterogeneous material structure where μ is constrained to vary in a range that is 0.5, 1, and 2 times the true μ range, as seen in scaled and non-dimensionalized versions of μ. Grey triangles represent the 20 surface observations, while the dashed black line indicates the shape of the true triangular material anomaly. Panel (d) shows the recovered material structure using the exponential function. Panel (e) displays the recovery of the fault slip, with the black solid line representing the true slip used to generate the synthetic surface data. The slip results from the joint inversion are shown as lines colored according to the different parameterizations of $\mu(\boldsymbol{m}_\mu)$.

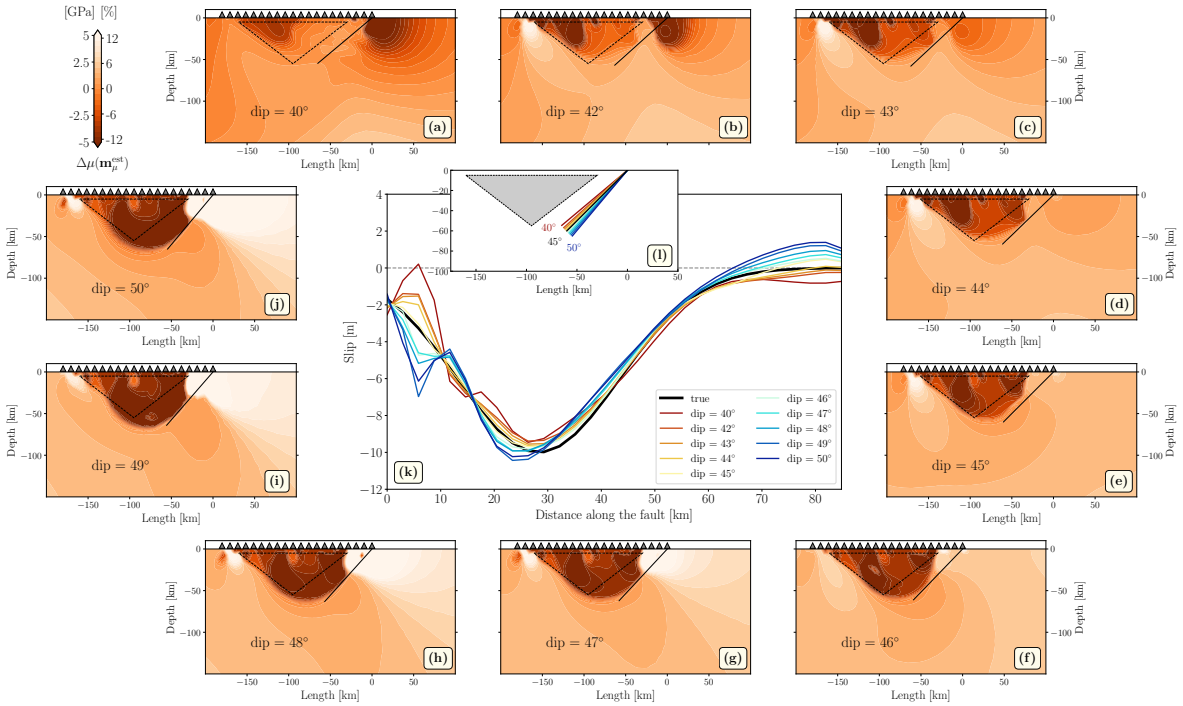

Figure 9. Results of joint inversion as a function of variations in the fault dip where μ inferences are provided in scales and non-dimensional versions. Panels (a) through (j) display the inferred heterogeneous material structure, similar to Fig. 6. Grey triangles represent the 20 surface observations, while the dashed black line indicates the shape of the true triangular material anomaly. Panel (k) shows the recovery of the fault slip. The black solid line indicates the true slip used to generate the synthetic surface data, whereas the slip results from the joint inversion are shown with lines colored according to different choices. The inset (panel j) provides a view of the triangular anomaly and the faults with different fault dips, represented by colored lines.

at shallow depths for shallower faults, while being over-predicted for deeper faults. In terms of the variations in the shear modulus structure, shallower faults yield poorer results compared to deeper faults, exhibiting some artifacts near the trench (panels a-c). On the other hand, deeper faults show better recovery of the triangular material anomaly (panels f through j). Near the trench, a trade-off between slip and shear modulus structure is observed locally. The underestimation of the slip distribution results in the inference of weaker materials (panels a-d), while the overestimation of slip indicates stronger material (panels f through j). This phenomenon is further evident in Fig. 7, where the presence of stronger materials (located to the right of the yellow star) corresponds to increased slip.

Overall, for our particular 2-D model setup, the triangular material anomaly is well recovered within approximately $\pm 5°$. We attempted the same joint inversion for fault dips below $40°$ or above $50°$, but inferring both model parameters proved to be more challenging. This challenge was anticipated by the observation that variations in fault dip can result in relatively large differences in surface displacements compared to the effects of heterogeneity (Fig. 2b,c). Thus, significant uncertainty in

fault geometry renders the joint inversion for slip and material structure ill-posed for these 2-D tests, indicating that there are simply inherent limits in the information that can be obtained, as in any inverse problem. In practice, relocated seismicity, for example, may provide quite detailed information on fault planes, and one might use other constraints, such as from radiated seismic waves, to infer fault slip independently to reduce non-uniqueness (e.g., Ide & Takeo 1997; Lay et al. 2011). Besides putting additional a priori constraints on joint slip and shear modulus inversions, it turns out that the 3-D geometry and data density of well-recorded coseismic deformation also makes the inversion quite a bit more robust, as will be explored in a companion application paper.

5 CONCLUSIONS

We developed and tested a novel technique, that employs an open-source modeling framework and adjoint-based inexact Newton method, to jointly invert geodetic data for fault slip and heterogeneous material properties, using the coseismic deformation and inversion for Poisson's ratio and shear modulus as a test case. This opens up a range of new applications to infer tectonically relevant signals and formally explore trade-offs between uncertainties in Earth properties and fault dynamics. Poisson's ratio anomalies for megathrust-like settings can be satisfactorily recovered from noisy data when the fault geometry and slip are known. The quality of our inverse results is primarily affected by the noise level of the surface observations, the number of available GNSS stations, and the earthquake source depth. Joint inversions for fault slip and shear modulus variations may be feasible for well-instrumented earthquakes. Our findings indicate that lateral variations in elastic strength can be recovered using geodetic data alone if fault geometries are reasonably well-known.

Beyond better constraining tectonic and volcano-associated dynamics, there is a broader need for flexible and transparent inverse methods to identify material parameters, with potential applications outside solid Earth including in hydrology, glaciology, and virtually any field of science. While we have focused on inverting static surface data from sparse GNSS stations, our approach shows promise for integrating other geodetic constraints, in particular, InSAR deformation time-series such as from Sentinel and the upcoming NISAR mission, and to expand the analysis to formal inversion of time-dependent processes, such as the complex transients observed during the seismic cycle.

ACKNOWLEDGMENTS

S.P., T.W.B, and D.L. were supported by NSF EAR-2121666, EAR-2045292, 19214743, and 1927216. U.V. and O.G. were supported by NSF ACI-1550593 and DOE ASCR DE-SC0019303.

DATA AVAILABILITY

The fully documented Jupyter notebooks for reproducing the results will be available for the readers in an online GitHub repository upon acceptance. We utilized FENICS-2019.1.0 and HIPPYLIB-3.0.0 to compute all the results in this study. These libraries can be downloaded at `https://fenicsproject.org` and `https://hippylib.github.io`, respectively. The unstructured meshes for the FE computations were generated using the open-source software GMSH (Geuzaine & Remacle 2009), and the corresponding files will be included in the online repository.

REFERENCES

Aagaard, B. T., Knepley, M. G., & Williams, C. A., 2013. A domain decomposition approach to implementing fault slip in finite-element models of quasi-static and dynamic crustal deformation, *J. Geophys. Res. Solid Earth*, **118**(6), 3059–3079.

Agata, R., Ichimura, T., Hori, T., Hirahara, K., Hashimoto, C., & Hori, M., 2017. An adjoint-based simultaneous estimation method of the asthenosphere's viscosity and afterslip using a fast and scalable finite-element adjoint solver, *Geophys. J. Int.*, **213**(1), 461–474.

Akçelik, V., Biros, G., Ghattas, O., Hill, J., Keyes, D., & van Bloemen Waanders, B., 2006. Parallel algorithms for PDE-constrained optimization, in *Parallel processing for scientific computing*, pp. 291–322, SIAM.

Alexanderian, A., Gloor, P. J., Ghattas, O., et al., 2016. On Bayesian A-and D-optimal experimental designs in infinite dimensions, *Bayesian Anal.*, **11**(3), 671–695.

Allgower, E. L., Böhmer, K., Potra, F. A., & Rheinboldt, W. C., 1986. A mesh-independence principle for operator equations and their discretizations, *SIAM J. Numer. Anal.*, **23**(1), 160–169.

Alnæs, M. S., Logg, A., Ølgaard, K. B., Rognes, M. E., & Wells, G. N., 2014. Unified form language: A domain-specific language for weak formulations of partial differential equations, *ACM Trans. Math. Software (TOMS)*, **40**(2), 1–37.

Arnold, D., Falk, R., & Winther, R., 2007. Mixed finite element methods for linear elasticity with weakly imposed symmetry, *Math. Comput.*, **76**(260), 1699–1723.

Arridge, S., Maass, P., Öktem, O., & Schönlieb, C., 2019. Solving inverse problems using data-driven models, *Acta Numerica*, **28**, 1–174.

Attia, A., Alexanderian, A., & Saibaba, A. K., 2018. Goal-oriented optimal design of experiments for large-scale Bayesian linear inverse problems, *Inverse Probl.*, **34**(9), 095009.

Avril, S., Bonnet, M., Bretelle, A.-S., Grédiac, M., Hild, F., Ienny, P., Latourte, F., Lemosse, D., Pagano, S., Pagnacco, E., et al., 2008. Overview of identification methods of mechanical parameters based on full-field measurements, *Exp. Mec.*, **48**, 381–402.

Balay, S., Abhyankar, S., Adams, M. F., Brown, J., Brune, P., Buschelman, K., Dalcin, L., Dener, A., Eijkhout, V., Gropp, W., et al., 2020. PETSc users manual revision 3.13, Tech. rep., Argonne National Lab.(ANL), Argonne, IL (United States).

Baumann, T. S., Kaus, B. J. P., & Popov, A. A., 2014. Constraining effective rheology through parallel joint geodynamic inversion, *Tectonophysics*, **631**, 197–211.

Benning, M. & Burger, M., 2018. Modern regularization methods for inverse problems, *Acta Numerica*, **27**, 1–111.

Beskos, A., Girolami, M., Lan, S., Farrell, P. E., & Stuart, A. M., 2017. Geometric MCMC for infinite-dimensional inverse problems, *J. Comput. Phys.*, **335**, 327–351.

Bonnet, M. & Constantinescu, A., 2005. Inverse problems in elasticity, *Inverse Probl.*, **21**(2), R1.

Borzì, A. & Schulz, V., 2011. *Computational optimization of systems governed by partial differential equations*, SIAM.

Brezzi, F., Douglas, J., & Marini, L. D., 1985. Two families of mixed finite elements for second order elliptic problems, *Numerische Mathematik*, **47**(2), 217–235.

Bui-Thanh, T. & Ghattas, O., 2013. Analysis of the Hessian for inverse scattering problems. Part III: Inverse medium scattering of electromagnetic waves in three dimensions, *Inverse Probl. Imaging*, **7**(4), 1139.

Bui-Thanh, T. & Ghattas, O., 2015. A scalable algorithm for MAP estimators in Bayesian inverse problems with Besov priors, *Inverse Probl. Imaging*, **9**(1), 27–53.

Bui-Thanh, T., Ghattas, O., Martin, J., & Stadler, G., 2013. A computational framework for infinite-dimensional Bayesian inverse problems Part I: The linearized case, with application to global seismic inversion, *SIAM J. Scient. Comp.*, **35**(6), A2494–A2523.

Bunge, H.-P., Hagelberg, C. R., & Travis, B. J., 2003. Mantle circulation models with variational data assimilation: inferring past mantle flow and structure from plate motion histories and seismic tomography, *Geophys. J. Int.*, **152**, 280–301.

Chan, T., Esedoglu, S., Park, F., Yip, A., et al., 2005. Recent developments in total variation image restoration, *Mathematical Models of Computer Vision*, **17**(2), 17–31.

Crawford, O., Al-Attar, D., Tromp, J., & Mitrovica, J. X., 2017. Forward and inverse modelling of post-seismic deformation, *Geophys. J. Int.*, pp. 845—876.

Dhar, S., Muto, J., Ito, Y., Miura, S., Moore, J. D. P., Ohta, Y., & Iinuma, T., 2022. Along-arc heterogeneous rheology inferred from post-seismic deformation of the 2011 Tohoku-oki earthquake, *Geophys. J. Int.*, **230**(1), 202–215.

Eisenstat, S. C. & Walker, H. F., 1996. Choosing the forcing terms in an inexact Newton method, *SIAM J. Scient. Comp.*, **17**(1), 16–32.

Engl, H. W., Hanke, M., & Neubauer, A., 1996. *Regularization of inverse problems*, vol. 375, Springer Science & Business Media.

Fatehiboroujeni, S., Petra, N., & Goyal, S., 2016. Towards adjoint-based inversion of the Lamé parameter field for slender structures with cantilever loading, in *International Design Engineering Technical Conferences and Computers and Information in Engineering Conference*, vol. 50206, p. V008T10A031, American Society of Mechanical Engineers.

Fatehiboroujeni, S., Petra, N., & Goyal, S., 2020. Linearized Bayesian inference for Young's modulus param-

eter field in an elastic model of slender structures, *Proc. Math. Phys. Eng. Sci.*, **476**(2238), 20190476.

Feigl, K. L. & Thatcher, W., 2006. Geodetic observations of post-seismic transients in the context of the earthquake deformation cycle, *Comptes Rendus Geoscience*, **338**, 1012–1028.

Geuzaine, C. & Remacle, J.-F., 2009. Gmsh: A 3-D finite element mesh generator with built-in pre-and post-processing facilities, *Int. J. Num. Meth. Eng.*, **79**(11), 1309–1331.

Ghattas, O. & Willcox, K., 2021. Learning physics-based models from data: perspectives from inverse problems and model reduction, *Acta Numerica*, **30**, 445–554.

Hadamard, J., 1923. Lectures on Cauchy's problem in linear partial differential equations, *Press. New Haven*.

Halko, N., Martinsson, P.-G., & Tropp, J. A., 2011. Finding structure with randomness: Probabilistic algorithms for constructing approximate matrix decompositions, *SIAM review*, **53**(2), 217–288.

Hashima, A., Becker, T. W., Freed, A. M., Sato, H., & Okaya, D. A., 2016. Coseismic deformation due to the 2011 Tohoku-oki earthquake: influence of 3-D elastic structure around Japan, *Earth, Planets and Space*, **68**(1), 1–15.

Hatanaka, Y., 2005. Evaluation of precision of routine solutions of GEONET, *J. Geogr. Surv. Inst.*, **108**, 49–56.

Heinkenschloss, M., 1993. Mesh independence for nonlinear least squares problems with norm constraints, *SIAM J. Opt.*, **3**(1), 81–117.

Ide, S. & Takeo, M., 1997. Determination of constitutive relations of fault slip based on seismic wave analysis, *J. Geophys. Res. Solid Earth*, **102**(B12), 27379–27391.

Iinuma, T., Hino, R., Kido, M., Inazu, D., Osada, Y., Ito, Y., Ohzono, M., Tsushima, H., Suzuki, S., Fujimoto, H., et al., 2012. Coseismic slip distribution of the 2011 off the Pacific coast of Tohoku earthquake (M9.0) refined by means of seafloor geodetic data, *J. Geophys. Res. Solid Earth*, **117**(B7).

Isaac, T., Petra, N., Stadler, G., & Ghattas, O., 2015. Scalable and efficient algorithms for the propagation of uncertainty from data through inference to prediction for large-scale problems, with application to flow of the Antarctic ice sheet, *J. Comput. Phys.*, **296**, 348–368.

Kelley, C. T. & Sachs, E. W., 1991. Mesh independence of Newton-like methods for infinite dimensional problems, *The Journal of Integral Equations and Applications*, pp. 549–573.

Koval, K., Alexanderian, A., & Stadler, G., 2020. Optimal experimental design under irreducible uncertainty for linear inverse problems governed by PDEs, *Inverse Probl.*, **36**(7), 075007.

Lawson, C. L. & Hanson, R. J., 1995. *Solving least squares problems*, SIAM.

Lay, T., Ammon, C. J., Kanamori, H., Xue, L., & Kim, M. J., 2011. Possible large near-trench slip during the 2011 Mw 9.0 off the Pacific coast of Tohoku earthquake, *Earth, Planets and Space*, **63**, 687–692.

Liu, L. & Gurnis, M., 2008. Simultaneous inversion of mantle properties and initial conditions using an adjoint of mantle convection, *J. Geophys. Res. Solid Earth*, **113**(B8).

Logg, A. & Wells, G. N., 2010. DOLFIN: Automated finite element computing, *ACM Trans. Math. Software (TOMS)*, **37**(2), 1–28.

Logg, A., Wells, G. N., & Hake, J., 2012. DOLFIN: A C++/Python finite element library, in *Automated solution of differential equations by the finite element method*, pp. 173–225, Springer.

Martin, J., Wilcox, L. C., Burstedde, C., & Ghattas, O., 2012. A stochastic Newton MCMC method for large-scale statistical inverse problems with application to seismic inversion, *SIAM J. Scient. Comp.*, **34**(3), A1460–A1487.

Melosh, H. J. & Raefsky, A., 1981. A simple and efficient method for introducing faults into finite element computations, *Bull. Seismol. Soc. Am.*, **71**(5), 1391–1400.

Miller, K., 1970. Least squares methods for ill-posed problems with a prescribed bound, *SIAM J. Math. Anal.*, **1**(1), 52–74.

Muto, J., Shibazaki, B., Iinuma, T., Ito, Y., Ohta, Y., Miura, S., & Nakai, Y., 2016. Heterogeneous rheology controlled postseismic deformation of the 2011 Tohoku-Oki earthquake, *Geophys. Res. Lett.*, **43**(10), 4971–4978.

Nocedal, J. & Wright, S. J., 1999. *Numerical optimization*, Springer.

Panuntun, H., Miyazaki, S., Fukuda, Y., & Orihara, Y., 2018. Probing the Poisson's ratio of poroelastic rebound following the 2011 Mw 9.0 Tohoku earthquake, *Geophys. J. Int.*, **215**(3), 2206–2221.

Pereverzev, S. & Schock, E., 2000. Morozov's discrepancy principle for Tikhonov, *Numerical Functional Analysis and Optimization*, **21**(7-8), 901–916.

Petra, N., Martin, J., Stadler, G., & Ghattas, O., 2014. A computational framework for infinite-dimensional Bayesian inverse problems, Part II: Stochastic Newton MCMC with application to ice sheet flow inverse problems, *SIAM J. Scient. Comp.*, **36**(4), A1525–A1555.

Puel, S., Khattatov, E., Villa, U., Liu, D., Ghattas, O., & Becker, T. W., 2022. A mixed, unified forward/inverse framework for earthquake problems: Fault implementation and coseismic slip estimate, *Geophys. J. Int.*, **230**(2), 733–758.

Rathgeber, F., Ham, D. A., Mitchell, L., Lange, M., Luporini, F., McRae, A. T. T., Bercea, G.-T., Markall, G. R., & Kelly, P. H. J., 2016. Firedrake: automating the finite element method by composing abstractions, *ACM Trans. Math. Software (TOMS)*, **43**(3), 1–27.

Reuber, G. S., 2021. Statistical and deterministic inverse methods in the geosciences: introduction, review, and application to the nonlinear diffusion equation, *GEM - Int. J. Geomath.*, **12**(1), 19.

Reuber, G. S., Holbach, L., Popov, A. A., Hanke, M., & Kaus, B. J. P., 2020. Inferring rheology and geometry of subsurface structures by adjoint-based inversion of principal stress directions, *Geophys. J. Int.*, **223**(2), 851–861.

Rudi, J., Gurnis, M., & Stadler, G., 2022. Simultaneous inference of plate boundary stresses and mantle rheology using adjoints: large-scale 2-D models, *Geophys. J. Int.*, **231**, 597–614.

Rudin, L. I., Osher, S., & Fatemi, E., 1992. Nonlinear total variation based noise removal algorithms, *Physica D: nonlinear phenomena*, **60**(1-4), 259–268.

Scherzer, O., 1993. The use of Morozov's discrepancy principle for Tikhonov regularization for solving nonlinear ill-posed problems, *Computing*, **51**(1), 45–60.

Steihaug, T., 1983. Local and superlinear convergence for truncated iterated projections methods, *Math. Program.*, **27**(2), 176–190.

Strong, D. & Chan, T., 2003. Edge-preserving and scale-dependent properties of total variation regularization, *Inverse Probl.*, **19**(6), S165.

Stuart, A. M., 2010. Inverse problems: a Bayesian perspective, *Acta Numerica*, **19**, 451–559.

Takada, Y. & Fukushima, Y., 2013. Volcanic subsidence triggered by the 2011 Tohoku earthquake in Japan, *Nat. Geosci.*, **6**(8), 637–641.

Tikhonov, A. N., 1963. Solution of incorrectly formulated problems and the regularization method, *Soviet Math.*, **4**, 1035–1038.

Tikhonov, A. N. & Arsenin, V. Y., 1977. Solutions of ill-posed problems.

Tröltzsch, F., 2010. *Optimal control of partial differential equations: theory, methods, and applications*, vol. 112, American Mathematical Soc.

Villa, U., Petra, N., & Ghattas, O., 2018. hIPPYlib: an Extensible Software Framework for Large-scale Deterministic and Bayesian Inverse Problems, *J. Open Source Software*, **3**(30).

Villa, U., Petra, N., & Ghattas, O., 2021. hIPPYlib: An Extensible Software Framework for Large-Scale Inverse Problems Governed by PDEs; Part I: Deterministic Inversion and Linearized Bayesian Inference, *ACM Trans. Math. Software (TOMS)*, **47**(2), 1–34.

Vogel, C. R., 2002. *Computational methods for inverse problems*, SIAM.

Williams, C. A. & Wallace, L. M., 2015. Effects of material property variations on slip estimates for subduction interface slow-slip events, *Geophys. Res. Lett.*, **42**(4), 1113–1121.

Williams, C. A. & Wallace, L. M., 2018. The impact of realistic elastic properties on inversions of shallow subduction interface slow slip events using seafloor geodetic data, *Geophys. Res. Lett.*, **45**(15), 7462–7470.

Wilson, C. R., Spiegelman, M., & van Keken, P. E., 2017. TerraFERMA: The Transparent Finite Element Rapid Model Assembler for multiphysics problems in Earth sciences, *Geochem. Geophys. Geosystems*, **18**(2), 769–810.

Worthen, J., Stadler, G., Petra, N., Gurnis, M., & Ghattas, O., 2014. Towards adjoint-based inversion for rheological parameters in nonlinear viscous mantle flow, *Phys. Earth Planet. Inter.*, **234**, 23–34.

Wu, K., Chen, P., & Ghattas, O., 2023. A fast and scalable computational framework for large-scale high-dimensional Bayesian optimal experimental design, *SIAM/ASA Journal on Uncertainty Quantification*, **11**(1), 235–261.

APPENDIX A: DERIVATION OF ELASTIC COMPLIANCE TENSOR FROM LAMÉ PARAMETERS TO YOUNG'S AND POISSON'S MODULI

In this section, we derive the expression of the elastic compliance tensor $\boldsymbol{A}$ from the Lamé parameters (μ and λ) to the shear and Poisson's ratio moduli, μ and ν. We start from the expression in Puel et al. (2022),

$$\boldsymbol{A}\boldsymbol{\sigma} = \frac{1}{2\mu}\left[\boldsymbol{\sigma} - \frac{\lambda}{2\mu + d\lambda}\mathrm{tr}(\boldsymbol{\sigma})\boldsymbol{I}\right]. \tag{A.1}$$

Knowing that the Lamé parameters can be written as a function of E and ν, respectively:

$$\lambda = \frac{E\nu}{(1+\nu)(1-2\nu)}, \qquad \mu = \frac{E}{2(1+\nu)}, \tag{A.2}$$

we can write:

$$\boldsymbol{A\sigma} = \frac{2(1+\nu)}{2E}\left[\boldsymbol{\sigma} - \frac{\frac{E\nu}{(1+\nu)(1-2\nu)}}{\frac{2E}{2(1+nu)} + \frac{dE\nu}{(1+\nu)(1-2\nu)}}\mathrm{tr}(\boldsymbol{\sigma})\boldsymbol{I}\right], \tag{A.3}$$

$$\boldsymbol{A\sigma} = \frac{1+\nu}{E}\left[\boldsymbol{\sigma} - \frac{\frac{E\nu}{(1+\nu)(1-2\nu)}}{\frac{E(1-2\nu)+dE\nu}{(1+\nu)(1-2\nu)}}\mathrm{tr}(\boldsymbol{\sigma})\boldsymbol{I}\right], \tag{A.4}$$

$$\boldsymbol{A\sigma} = \frac{1+\nu}{E}\left[\boldsymbol{\sigma} - \frac{E\nu}{E(1-2\nu)+dE\nu}\mathrm{tr}(\boldsymbol{\sigma})\boldsymbol{I}\right], \tag{A.5}$$

$$\boldsymbol{A\sigma} = \frac{1+\nu}{E}\left[\boldsymbol{\sigma} - \frac{E\nu}{E-2E\nu+dE\nu}\mathrm{tr}(\boldsymbol{\sigma})\boldsymbol{I}\right], \tag{A.6}$$

$$\boldsymbol{A\sigma} = \frac{1+\nu}{E}\left[\boldsymbol{\sigma} - \frac{E\nu}{E(1-2\nu+d\nu)}\mathrm{tr}(\boldsymbol{\sigma})\boldsymbol{I}\right], \tag{A.7}$$

$$\boldsymbol{A\sigma} = \frac{1+\nu}{E}\left[\boldsymbol{\sigma} - \frac{\nu}{1+\nu(d-2)}\mathrm{tr}(\boldsymbol{\sigma})\boldsymbol{I}\right], \tag{A.8}$$

$$\boldsymbol{A\sigma} = \frac{1}{2\mu}\left[\boldsymbol{\sigma} - \frac{\nu}{1+\nu(d-2)}\mathrm{tr}(\boldsymbol{\sigma})\boldsymbol{I}\right]. \tag{A.9}$$

In particular, for the two-dimensional ($d = 2$) problems considered in this work, the expression reads:

$$\boldsymbol{A\sigma} = \frac{1}{2\mu}\boldsymbol{\sigma} - \frac{\nu}{2\mu}\mathrm{tr}(\boldsymbol{\sigma})\boldsymbol{I}. \tag{A.10}$$

APPENDIX B: GRADIENT AND HESSIAN COMPUTATIONS FOR THE POISSON'S RATIO INVERSE PROBLEM

Here, we derive the gradient and Hessian expressions through variational calculus and the adjoint method. Using the Lagrangian formalism (Tröltzsch 2010) we formulate an expression for the gradient $\mathcal{G}(\boldsymbol{m})$ at any arbitrary point in parameter space. The Lagrangian functional for the gradient $\mathcal{L}^{\mathcal{G}}$ includes eq. (4) and the weak form of the forward problem (eq. 3),

$$\begin{aligned}
\mathcal{L}^{\mathcal{G}}(\boldsymbol{\sigma}, \boldsymbol{u}, \boldsymbol{r}, \boldsymbol{m}, \boldsymbol{\tau}, \boldsymbol{\omega}, \boldsymbol{\xi}) = {} & \frac{1}{2}\int_{\Omega}(\mathcal{B}\boldsymbol{u} - \mathbf{d})^T \boldsymbol{\Gamma}_{\text{noise}}^{-1}(\mathcal{B}\boldsymbol{u} - \mathbf{d})\, d\boldsymbol{x} + \mathcal{R}(\boldsymbol{m}) \\
& + \int_{\Omega}\frac{1}{2\mu}\left[\boldsymbol{\sigma} - \frac{\nu(\boldsymbol{m})}{1+\nu(\boldsymbol{m})(d-2)}\,\mathrm{tr}(\boldsymbol{\sigma})\boldsymbol{I}\right] : \boldsymbol{\tau}\,\mathrm{d}\boldsymbol{x} \\
& + \int_{\Omega}\boldsymbol{u}\cdot(\nabla\cdot\boldsymbol{\tau})\,\mathrm{d}\boldsymbol{x} + \int_{\Omega}\mathrm{as}(\boldsymbol{\tau})\cdot\boldsymbol{r}\,\mathrm{d}\boldsymbol{x} \\
& - \int_{\Gamma_D}\boldsymbol{u}_0\cdot(\boldsymbol{\tau}\,\mathbf{n})\,\mathrm{d}\boldsymbol{s} - \int_{\Gamma_F}\boldsymbol{s}\cdot\left[T(\mathbf{n}_{\Gamma_F})(\boldsymbol{\tau}\,\mathbf{n}_{\Gamma_F})\right]\mathrm{d}\boldsymbol{S} \\
& + \int_{\Omega}(\nabla\cdot\boldsymbol{\sigma})\cdot\boldsymbol{\omega}\,\mathrm{d}\boldsymbol{x} + \int_{\Omega}\boldsymbol{f}\cdot\boldsymbol{\omega}\,\mathrm{d}\boldsymbol{x} + \int_{\Omega}\mathrm{as}(\boldsymbol{\sigma})\cdot\boldsymbol{\xi}\,\mathrm{d}\boldsymbol{x},
\end{aligned} \tag{B.1}$$

where the second term can be a Tikhonov-type regularization which imposes some smoothness of the solution $\boldsymbol{m}$. $\boldsymbol{\tau}$, $\boldsymbol{\omega}$ and $\boldsymbol{\xi}$ are the adjoint variables for the stress, displacement and rotation, respectively.

By taking the derivative of $\mathcal{L}^{\mathcal{G}}$ with respect to the adjoint and the state variables we obtain the variational form of the forward and adjoint equations, respectively. The latter reads:

$$\begin{aligned}\left(\frac{\partial \mathcal{L}^{\mathcal{G}}}{\partial \boldsymbol{\sigma}}, \tilde{\boldsymbol{\sigma}}\right) + \left(\frac{\partial \mathcal{L}^{\mathcal{G}}}{\partial \boldsymbol{u}}, \tilde{\boldsymbol{u}}\right) + \left(\frac{\partial \mathcal{L}^{\mathcal{G}}}{\partial \boldsymbol{r}}, \tilde{\boldsymbol{r}}\right) &= \int_{\Omega} \frac{1}{2\mu}\big[\tilde{\boldsymbol{\sigma}} - \frac{\nu(\boldsymbol{m})}{1+\nu(\boldsymbol{m})(d-2)}\operatorname{tr}(\tilde{\boldsymbol{\sigma}})\boldsymbol{I}\big] : \boldsymbol{\tau}\,\mathrm{d}\boldsymbol{x} \\ &+ \int_{\Omega} (\nabla\cdot\tilde{\boldsymbol{\sigma}})\cdot\boldsymbol{\omega}\,\mathrm{d}\boldsymbol{x} + \int_{\Omega}\operatorname{as}(\tilde{\boldsymbol{\sigma}})\cdot\boldsymbol{\xi}\,\mathrm{d}\boldsymbol{x} \\ &+ \int_{\Omega}\tilde{\boldsymbol{u}}\cdot(\nabla\cdot\boldsymbol{\tau})\,\mathrm{d}\boldsymbol{x} + \int_{\Omega}\operatorname{as}(\boldsymbol{\tau})\cdot\tilde{\boldsymbol{r}}\,\mathrm{d}\boldsymbol{x} \\ &+ \int_{\Omega}\mathcal{B}^{*}\boldsymbol{\Gamma}_{\text{noise}}^{-1}\big(\mathcal{B}\boldsymbol{u}-\mathbf{d}\big)\cdot\tilde{\boldsymbol{u}}\,\mathrm{d}\boldsymbol{x} = 0 \\ &\forall\tilde{\boldsymbol{\sigma}}\in\Sigma;\ \forall\tilde{\boldsymbol{u}}\in W;\ \forall\tilde{\boldsymbol{r}}\in\Xi,\end{aligned} \tag{B.2}$$

where $\mathcal{B}^{*}$ is the inverse mapping of the observational operator which maps the discrete surface displacement back to the infinite-dimensional state space, and $\tilde{\boldsymbol{\sigma}}$, $\tilde{\boldsymbol{u}}$, and $\tilde{\boldsymbol{r}}$ are test functions. Solving eq. (6) gives the adjoint variables $\boldsymbol{\tau}$, $\boldsymbol{\omega}$ and $\boldsymbol{\xi}$. By integrating the second term by parts, we can derive the strong form of the adjoint problem:

$$\begin{cases} A(\boldsymbol{m})\,\boldsymbol{\tau} - \nabla\boldsymbol{\omega} + \operatorname{as}^{*}(\boldsymbol{\xi}) = \mathbf{0} & \text{in } \Omega, \\ \nabla\cdot\boldsymbol{\tau} = -\mathcal{B}^{*}\boldsymbol{\Gamma}_{\text{noise}}^{-1}\big(\mathcal{B}\boldsymbol{u}-\mathbf{d}\big) & \text{in } \Omega, \\ \operatorname{as}(\boldsymbol{\tau}) = \mathbf{0} & \text{in } \Omega, \\ \boldsymbol{\omega} = \mathbf{0} & \text{on } \Gamma_D, \\ \boldsymbol{\tau}\cdot\mathbf{n} = \mathbf{0} & \text{on } \Gamma_N, \end{cases} \tag{B.3}$$

where the compliance elastic tensor $A(\boldsymbol{m})$ depends non-linearly on the Poisson's ratio $\boldsymbol{m}$ (eq. 2), and $\operatorname{as}^{*}(\boldsymbol{\xi})$ is defined as:

$$\operatorname{as}^{*}(\boldsymbol{\xi}) = \begin{pmatrix} 0 & -\xi \\ \xi & 0 \end{pmatrix}. \tag{B.4}$$

The infinite-dimensional gradient, which is the Gâteaux derivative of the objective function $\mathcal{J}(\boldsymbol{m})$ with respect to $\boldsymbol{m}$, can be derived by taking a variation of the Lagrangian functional with respect to the model parameter. The gradient expression in a arbitrary direction $\tilde{\boldsymbol{m}}$ reads:

$$(\mathcal{G}(\boldsymbol{m}), \tilde{\boldsymbol{m}}) = (\mathcal{R}_m(\boldsymbol{m}), \tilde{\boldsymbol{m}}) - \frac{1}{2\mu}\int_{\Omega}\frac{\nu_m(\boldsymbol{m})\,\tilde{\boldsymbol{m}}}{\big[1+\nu(\boldsymbol{m})(d-2)\big]^2}\operatorname{tr}(\boldsymbol{\sigma})\boldsymbol{I} : \boldsymbol{\tau}\,\mathrm{d}\boldsymbol{x} \qquad \forall\tilde{\boldsymbol{m}}\in\mathcal{M}, \tag{B.5}$$

where $(\mathcal{R}_m(\boldsymbol{m}), \tilde{\boldsymbol{m}})$ denotes the Gâteaux derivative of $\mathcal{R}$ with respect to $\boldsymbol{m}$ in the direction $\tilde{\boldsymbol{m}}$. $\nu_m(\boldsymbol{m})$ indicates the derivative of $\nu(\boldsymbol{m})$ with respect to $\boldsymbol{m}$. $\boldsymbol{\sigma}$ and $\boldsymbol{\tau}$ are the solutions of the forward and adjoint problems (eqs. 1 and B.3), respectively. The cost of evaluating the gradient consists of one forward and one adjoint PDE solve.

For the derivation of the Hessian action, we repeat the same process as before and construct the second-order Lagrangian functional $\mathcal{L}^{\mathcal{H}}$ as the sum of gradient, state and adjoint equations, respectively:

$$
\begin{aligned}
&\mathcal{L}^{\mathcal{H}}(\boldsymbol{\sigma}, \boldsymbol{u}, \boldsymbol{r}, \boldsymbol{m}, \boldsymbol{\tau}, \boldsymbol{\omega}, \boldsymbol{\xi}, \hat{\boldsymbol{\sigma}}, \hat{\boldsymbol{u}}, \hat{\boldsymbol{r}}, \hat{\boldsymbol{m}}, \hat{\boldsymbol{\tau}}, \hat{\boldsymbol{\omega}}, \hat{\boldsymbol{\xi}}) \\
&\qquad = (\mathcal{R}_m(\boldsymbol{m}), \hat{\boldsymbol{m}}) - \frac{1}{2\mu} \int_\Omega \frac{\nu_m(\boldsymbol{m})\, \hat{\boldsymbol{m}}}{\big[1 + \nu(\boldsymbol{m})(d-2)\big]^2} \mathrm{tr}(\boldsymbol{\sigma}) \boldsymbol{I} : \boldsymbol{\tau} \, \mathrm{d}\boldsymbol{x} \\
&\qquad + \int_\Omega \frac{1}{2\mu} \big[\boldsymbol{\sigma} - \frac{\nu(\boldsymbol{m})}{1 + \nu(\boldsymbol{m})(d-2)} \, \mathrm{tr}(\boldsymbol{\sigma}) \boldsymbol{I}\big] : \hat{\boldsymbol{\tau}} \, \mathrm{d}\boldsymbol{x} \\
&\qquad + \int_\Omega \boldsymbol{u} \cdot (\nabla \cdot \hat{\boldsymbol{\tau}}) \, \mathrm{d}\boldsymbol{x} + \int_\Omega \mathrm{as}(\hat{\boldsymbol{\tau}}) \cdot \boldsymbol{r} \, \mathrm{d}\boldsymbol{x} \\
&\qquad - \int_{\Gamma_F} \boldsymbol{s} \cdot \big[T(\mathbf{n}_{\Gamma_F})(\hat{\boldsymbol{\tau}}\, \mathbf{n}_{\Gamma_F})\big] \, \mathrm{d}\boldsymbol{S} - \int_{\Gamma_D} \boldsymbol{u}_0 \cdot (\hat{\boldsymbol{\tau}}\, \mathbf{n}) \, \mathrm{d}\boldsymbol{s} \\
&\qquad + \int_\Omega (\nabla \cdot \boldsymbol{\sigma}) \cdot \hat{\boldsymbol{\omega}} \, \mathrm{d}\boldsymbol{x} + \int_\Omega \boldsymbol{f} \cdot \hat{\boldsymbol{\omega}} \, \mathrm{d}\boldsymbol{x} + \int_\Omega \mathrm{as}(\boldsymbol{\sigma}) \cdot \hat{\boldsymbol{\xi}} \, \mathrm{d}\boldsymbol{x} \\
&\qquad + \int_\Omega \frac{1}{2\mu} \big[\hat{\boldsymbol{\sigma}} - \frac{\nu(\boldsymbol{m})}{1 + \nu(\boldsymbol{m})(d-2)} \, \mathrm{tr}(\hat{\boldsymbol{\sigma}}) \boldsymbol{I}\big] : \boldsymbol{\tau} \, \mathrm{d}\boldsymbol{x} \\
&\qquad + \int_\Omega (\nabla \cdot \hat{\boldsymbol{\sigma}}) \cdot \boldsymbol{\omega} \, \mathrm{d}\boldsymbol{x} + \int_\Omega \mathrm{as}(\hat{\boldsymbol{\sigma}}) \cdot \boldsymbol{\xi} \, \mathrm{d}\boldsymbol{x} + \int_\Omega \mathrm{as}(\boldsymbol{\tau}) \cdot \hat{\boldsymbol{r}} \, \mathrm{d}\boldsymbol{x} \\
&\qquad + \int_\Omega \hat{\boldsymbol{u}} \cdot (\nabla \cdot \boldsymbol{\tau}) \, \mathrm{d}\boldsymbol{x} + \int_\Omega \mathcal{B}^* \boldsymbol{\Gamma}_{\mathrm{noise}}^{-1} \big(\mathcal{B}\boldsymbol{u} - \mathbf{d}\big) \cdot \hat{\boldsymbol{u}} \, \mathrm{d}\boldsymbol{x}.
\end{aligned}
\tag{B.6}
$$

To obtain the action of the Hessian in a direction $\hat{\boldsymbol{m}}$ we take the derivative of $\mathcal{L}^{\mathcal{H}}$ with respect to $\boldsymbol{m}$:

$$
\begin{aligned}
&(\tilde{\boldsymbol{m}}, \mathcal{H}(\boldsymbol{m})\, \hat{\boldsymbol{m}}) = (\tilde{\boldsymbol{m}}, \mathcal{R}_{mm}(\boldsymbol{m})\, \hat{\boldsymbol{m}}) \\
&\qquad - \frac{1}{2\mu} \int_\Omega \frac{\big[\nu_{mm}(\boldsymbol{m}) + 2\nu_m^2(\boldsymbol{m})(d-2)\big]}{\big[1 + \nu(\boldsymbol{m})(d-2)\big]^2} \, \tilde{\boldsymbol{m}} \hat{\boldsymbol{m}} \, \mathrm{tr}(\boldsymbol{\sigma}) \boldsymbol{I} : \boldsymbol{\tau} \, \mathrm{d}\boldsymbol{x} \\
&\qquad - \frac{1}{2\mu} \int_\Omega \frac{\nu_m(\boldsymbol{m})\, \tilde{\boldsymbol{m}}}{\big[1 + \nu(\boldsymbol{m})(d-2)\big]^2} \big[\mathrm{tr}(\boldsymbol{\sigma}) \boldsymbol{I} : \hat{\boldsymbol{\tau}} + \mathrm{tr}(\hat{\boldsymbol{\sigma}}) \boldsymbol{I} : \boldsymbol{\tau}\big] \, \mathrm{d}\boldsymbol{x} \qquad \forall \tilde{\boldsymbol{m}} \in \mathcal{M},
\end{aligned}
\tag{B.7}
$$

where $\boldsymbol{\sigma}$ and $\boldsymbol{\tau}$ are the solutions to the forward and adjoint problems in eqs. (1) and (B.3), respectively, and $\hat{\boldsymbol{\sigma}}$ and $\hat{\boldsymbol{\tau}}$ are the solutions of the incremental forward and adjoint problems, respectively. The incremental forward equation is given by the derivative of the second-order Lagrangian with respect

to the adjoint variables, and reads:

$$\begin{aligned}\left(\frac{\partial\mathcal{L}^{\mathcal{H}}}{\partial\boldsymbol{\tau}},\tilde{\boldsymbol{\tau}}\right)+\left(\frac{\partial\mathcal{L}^{\mathcal{H}}}{\partial\boldsymbol{\omega}},\tilde{\boldsymbol{\omega}}\right)+\left(\frac{\partial\mathcal{L}^{\mathcal{H}}}{\partial\boldsymbol{\xi}},\tilde{\boldsymbol{\xi}}\right) &= \int_\Omega \hat{\boldsymbol{u}}\cdot(\nabla\cdot\tilde{\boldsymbol{\tau}})\,\mathrm{d}\boldsymbol{x}+\int_\Omega \mathrm{as}(\tilde{\boldsymbol{\tau}})\cdot\hat{\boldsymbol{r}}\,\mathrm{d}\boldsymbol{x}\\ &-\frac{1}{2\mu}\int_\Omega\frac{\nu_m(\boldsymbol{m})\,\hat{\boldsymbol{m}}}{\left[1+\nu(\boldsymbol{m})(d-2)\right]^2}\mathrm{tr}(\boldsymbol{\sigma})\boldsymbol{I}:\tilde{\boldsymbol{\tau}}\,\mathrm{d}\boldsymbol{x}\\ &+\int_\Omega\frac{1}{2\mu}\Big[\hat{\boldsymbol{\sigma}}-\frac{\nu(\boldsymbol{m})}{1+\nu(\boldsymbol{m})(d-2)}\,\mathrm{tr}(\hat{\boldsymbol{\sigma}})\boldsymbol{I}\Big]:\tilde{\boldsymbol{\tau}}\,\mathrm{d}\boldsymbol{x}\\ &+\int_\Omega(\nabla\cdot\hat{\boldsymbol{\sigma}})\cdot\tilde{\boldsymbol{\omega}}\,\mathrm{d}\boldsymbol{x}+\int_\Omega\mathrm{as}(\hat{\boldsymbol{\sigma}})\cdot\tilde{\boldsymbol{\xi}}\,\mathrm{d}\boldsymbol{x}=0\\ &\quad\forall\tilde{\boldsymbol{\tau}}\in\Sigma;\ \forall\tilde{\boldsymbol{\omega}}\in W;\ \forall\tilde{\boldsymbol{\xi}}\in\Xi,\end{aligned}\tag{B.8}$$

while, by taking the variation of $\mathcal{L}^{\mathcal{H}}$ with respect to the state variables, the incremental adjoint equation reads:

$$\begin{aligned}\left(\frac{\partial\mathcal{L}^{\mathcal{H}}}{\partial\boldsymbol{\sigma}},\tilde{\boldsymbol{\sigma}}\right)+\left(\frac{\partial\mathcal{L}^{\mathcal{H}}}{\partial\boldsymbol{u}},\tilde{\boldsymbol{u}}\right)+\left(\frac{\partial\mathcal{L}^{\mathcal{H}}}{\partial\boldsymbol{r}},\tilde{\boldsymbol{r}}\right) &= \int_\Omega(\nabla\cdot\tilde{\boldsymbol{\sigma}})\cdot\hat{\boldsymbol{\omega}}\,\mathrm{d}\boldsymbol{x}+\int_\Omega\mathrm{as}(\tilde{\boldsymbol{\sigma}})\cdot\hat{\boldsymbol{\xi}}\,\mathrm{d}\boldsymbol{x}\\ &-\frac{1}{2\mu}\int_\Omega\frac{\nu_m(\boldsymbol{m})\,\hat{\boldsymbol{m}}}{\left[1+\nu(\boldsymbol{m})(d-2)\right]^2}\mathrm{tr}(\tilde{\boldsymbol{\sigma}})\boldsymbol{I}:\boldsymbol{\tau}\,\mathrm{d}\boldsymbol{x}\\ &+\int_\Omega\frac{1}{2\mu}\Big[\tilde{\boldsymbol{\sigma}}-\frac{\nu(\boldsymbol{m})}{1+\nu(\boldsymbol{m})(d-2)}\,\mathrm{tr}(\tilde{\boldsymbol{\sigma}})\boldsymbol{I}\Big]:\hat{\boldsymbol{\tau}}\,\mathrm{d}\boldsymbol{x}\\ &+\int_\Omega\tilde{\boldsymbol{u}}\cdot(\nabla\cdot\hat{\boldsymbol{\tau}})\,\mathrm{d}\boldsymbol{x}+\int_\Omega\mathcal{B}^*\boldsymbol{\Gamma}_{\mathrm{noise}}^{-1}\mathcal{B}\tilde{\boldsymbol{u}}\cdot\hat{\boldsymbol{u}}\,\mathrm{d}\boldsymbol{x}\\ &+\int_\Omega\mathrm{as}(\hat{\boldsymbol{\tau}})\cdot\tilde{\boldsymbol{r}}\,\mathrm{d}\boldsymbol{x}=0\\ &\quad\forall\tilde{\boldsymbol{\sigma}}\in\Sigma;\ \forall\tilde{\boldsymbol{u}}\in W;\ \forall\tilde{\boldsymbol{r}}\in\Xi.\end{aligned}\tag{B.9}$$

APPENDIX C: GRADIENT AND HESSIAN COMPUTATIONS FOR THE JOINT INVERSE PROBLEM

Similarly to the Poisson's ratio inverse problem, we can derive the gradient and Hessian expressions by building the first and second-order Lagrangian functionals, respectively (Tröltzsch 2010). In this case, we need to consider the contribution of both the slip component $\boldsymbol{m}_s$ and the shear modulus structure $\mu(\boldsymbol{m}_\mu)$. The Lagrangian functional for the gradient $\mathcal{L}^{\mathcal{G}}$ includes eq. (4) and the weak form

of the forward problem (eq. 3),

$$\begin{aligned}\mathcal{L}^{\mathcal{G}}(\boldsymbol{\sigma},\boldsymbol{u},\boldsymbol{r},\boldsymbol{m}_\mu,\boldsymbol{m}_s,\boldsymbol{\tau},\boldsymbol{\omega},\boldsymbol{\xi}) &= \frac{1}{2}\int_\Omega (\mathcal{B}\boldsymbol{u}-\mathbf{d})^T\,\boldsymbol{\Gamma}_{\text{noise}}^{-1}\,(\mathcal{B}\boldsymbol{u}-\mathbf{d})\,\mathrm{d}\boldsymbol{x} + \mathcal{R}(\boldsymbol{m}_\mu)+\mathcal{R}(\boldsymbol{m}_s)\\ &+\int_\Omega \frac{1}{2\mu(\boldsymbol{m}_\mu)}\big[\boldsymbol{\sigma}-\frac{\nu}{1+\nu(d-2)}\,\mathrm{tr}(\boldsymbol{\sigma})\boldsymbol{I}\big]:\boldsymbol{\tau}\,\mathrm{d}\boldsymbol{x}\\ &+\int_\Omega \boldsymbol{u}\cdot(\nabla\cdot\boldsymbol{\tau})\,\mathrm{d}\boldsymbol{x}+\int_\Omega \mathrm{as}(\boldsymbol{\tau})\cdot\boldsymbol{r}\,\mathrm{d}\boldsymbol{x}\\ &-\int_{\Gamma_D}\boldsymbol{u}_0\cdot(\boldsymbol{\tau}\,\mathbf{n})\,\mathrm{d}\boldsymbol{s}-\int_{\Gamma_F}\boldsymbol{m}_s\cdot\big[T(\mathbf{n}_{\Gamma_F})(\boldsymbol{\tau}\,\mathbf{n}_{\Gamma_F})\big]\,\mathrm{d}\boldsymbol{S}\\ &+\int_\Omega(\nabla\cdot\boldsymbol{\sigma})\cdot\boldsymbol{\omega}\,\mathrm{d}\boldsymbol{x}+\int_\Omega\boldsymbol{f}\cdot\boldsymbol{\omega}\,\mathrm{d}\boldsymbol{x}+\int_\Omega\mathrm{as}(\boldsymbol{\sigma})\cdot\boldsymbol{\xi}\,\mathrm{d}\boldsymbol{x},\end{aligned}\tag{C.1}$$

where d is the problem dimension (2-3D). $\boldsymbol{\tau}$, $\boldsymbol{\omega}$ and $\boldsymbol{\xi}$ are the adjoint variables for the stress, displacement and rotation, respectively. By taking the derivative of $\mathcal{L}^{\mathcal{G}}$ with respect to the adjoint and the state variables we obtain the variational form of the forward and adjoint equations, respectively. The latter reads:

$$\begin{aligned}\Big(\frac{\partial\mathcal{L}^{\mathcal{G}}}{\partial\boldsymbol{\sigma}},\tilde{\boldsymbol{\sigma}}\Big)+\Big(\frac{\partial\mathcal{L}^{\mathcal{G}}}{\partial\boldsymbol{u}},\tilde{\boldsymbol{u}}\Big)+\Big(\frac{\partial\mathcal{L}^{\mathcal{G}}}{\partial\boldsymbol{r}},\tilde{\boldsymbol{r}}\Big) &= \int_\Omega\frac{1}{2\mu(\boldsymbol{m}_\mu)}\big[\tilde{\boldsymbol{\sigma}}-\frac{\nu}{1+\nu(d-2)}\,\mathrm{tr}(\tilde{\boldsymbol{\sigma}})\boldsymbol{I}\big]:\boldsymbol{\tau}\,\mathrm{d}\boldsymbol{x}\\ &+\int_\Omega(\nabla\cdot\tilde{\boldsymbol{\sigma}})\cdot\boldsymbol{\omega}\,\mathrm{d}\boldsymbol{x}+\int_\Omega\mathrm{as}(\tilde{\boldsymbol{\sigma}})\cdot\boldsymbol{\xi}\,\mathrm{d}\boldsymbol{x}\\ &+\int_\Omega\tilde{\boldsymbol{u}}\cdot(\nabla\cdot\boldsymbol{\tau})\,\mathrm{d}\boldsymbol{x}+\int_\Omega\mathrm{as}(\boldsymbol{\tau})\cdot\tilde{\boldsymbol{r}}\,\mathrm{d}\boldsymbol{x}\\ &+\int_\Omega\mathcal{B}^*\boldsymbol{\Gamma}_{\text{noise}}^{-1}\big(\mathcal{B}\boldsymbol{u}-\mathbf{d}\big)\cdot\tilde{\boldsymbol{u}}\,\mathrm{d}\boldsymbol{x}=0\\ &\forall\tilde{\boldsymbol{\sigma}}\in\Sigma;\ \forall\tilde{\boldsymbol{u}}\in W;\ \forall\tilde{\boldsymbol{r}}\in\Xi,\end{aligned}\tag{C.2}$$

where $\mathcal{B}^*$ is the inverse mapping of the observational operator which maps the discrete surface displacement back to the infinite-dimensional state space, and $\tilde{\boldsymbol{\sigma}}$, $\tilde{\boldsymbol{u}}$, and $\tilde{\boldsymbol{r}}$ are test functions. Solving eq. (C.2) gives the adjoint variables $\boldsymbol{\tau}$, $\boldsymbol{\omega}$ and $\boldsymbol{\xi}$. The strong form of the adjoint equation reads the same as eq. (B.3) when $A(\boldsymbol{m})$ is substituted by $A(\boldsymbol{m}_\mu)$. Note that the adjoint equation does not depend on the fault parameter $\boldsymbol{m}_s$.

By taking the derivative of the Lagrangian functional of the gradient with respect to the model parameters $(\boldsymbol{m}_\mu,\boldsymbol{m}_s)$, we obtain the gradient expression in a arbitrary direction $(\tilde{\boldsymbol{m}}_\mu,\tilde{\boldsymbol{m}}_s)$:

$$\begin{aligned}\big(\mathcal{G}(\boldsymbol{m}_\mu,\boldsymbol{m}_s),(\tilde{\boldsymbol{m}}_\mu,\tilde{\boldsymbol{m}}_s)\big) &= (\mathcal{R}_{m_\mu}(\boldsymbol{m}_\mu),\tilde{\boldsymbol{m}}_\mu)+(\mathcal{R}_{m_s}(\boldsymbol{m}_s),\tilde{\boldsymbol{m}}_s)\\ &+\int_\Omega\frac{\mu_m(\boldsymbol{m}_\mu)\tilde{\boldsymbol{m}}_\mu}{2\mu^2(\boldsymbol{m}_\mu)}\big[\boldsymbol{\sigma}-\frac{\nu}{1+\nu(d-2)}\,\mathrm{tr}(\boldsymbol{\sigma})\boldsymbol{I}\big]:\boldsymbol{\tau}\,\mathrm{d}\boldsymbol{x}\\ &-\int_{\Gamma_F}\tilde{\boldsymbol{m}}_s\cdot\big[T(\mathbf{n}_{\Gamma_F})(\boldsymbol{\tau}\,\mathbf{n}_{\Gamma_F})\big]\,\mathrm{d}\boldsymbol{S}\qquad\forall(\tilde{\boldsymbol{m}}_\mu,\tilde{\boldsymbol{m}}_s)\in\mathcal{M},\end{aligned}\tag{C.3}$$

where μ_m is the derivative of $\mu(\boldsymbol{m}_\mu)$ with respect to $\boldsymbol{m}_\mu$, and $\mathcal{R}_{m_\mu}(\boldsymbol{m}_\mu)$ and $\mathcal{R}_{m_s}(\boldsymbol{m}_s)$ are the

derivatives of the regularization of the shear modulus and fault slip with respect to $\boldsymbol{m}_\mu$ and $\boldsymbol{m}_s$, respectively.

To find the expression of the Hessian action in a direction $(\hat{\boldsymbol{m}}_\mu, \hat{\boldsymbol{m}}_s)$, we need to build the second-order Lagrangian functional $\mathcal{L}^{\mathcal{H}}$ of the joint inverse problem. This is composed of the sum of the gradient expression (eq. C.3), state and adjoint equations, respectively, and reads:

$$
\begin{aligned}
&\mathcal{L}^{\mathcal{H}}(\boldsymbol{\sigma}, \boldsymbol{u}, \boldsymbol{r}, \boldsymbol{m}_\mu, \boldsymbol{m}_s, \boldsymbol{\tau}, \boldsymbol{\omega}, \boldsymbol{\xi}, \hat{\boldsymbol{\sigma}}, \hat{\boldsymbol{u}}, \hat{\boldsymbol{r}}, \hat{\boldsymbol{m}}_\mu, \hat{\boldsymbol{m}}_s, \hat{\boldsymbol{\tau}}, \hat{\boldsymbol{\omega}}, \hat{\boldsymbol{\xi}}) \\
&\qquad = (\mathcal{R}_{m_\mu}(\boldsymbol{m}_\mu), \hat{\boldsymbol{m}}_\mu) + (\mathcal{R}_{m_s}(\boldsymbol{m}_s), \hat{\boldsymbol{m}}_s) \\
&\qquad + \int_\Omega \frac{\mu_m(\boldsymbol{m}_\mu)\tilde{\boldsymbol{m}}_\mu}{2\mu^2(\boldsymbol{m}_\mu)} \big[\boldsymbol{\sigma} - \frac{\nu}{1+\nu(d-2)} \operatorname{tr}(\boldsymbol{\sigma})\boldsymbol{I}\big] : \boldsymbol{\tau} \,\mathrm{d}\boldsymbol{x} \\
&\qquad - \int_{\Gamma_F} \hat{\boldsymbol{m}}_s \cdot \big[T(\mathbf{n}_{\Gamma_F})(\boldsymbol{\tau}\,\mathbf{n}_{\Gamma_F})\big] \,\mathrm{d}\boldsymbol{S} \\
&\qquad + \int_\Omega \frac{1}{2\mu(\boldsymbol{m}_\mu)} \big[\boldsymbol{\sigma} - \frac{\nu}{1+\nu(d-2)} \operatorname{tr}(\boldsymbol{\sigma})\boldsymbol{I}\big] : \hat{\boldsymbol{\tau}} \,\mathrm{d}\boldsymbol{x} \\
&\qquad + \int_\Omega \boldsymbol{u} \cdot (\nabla \cdot \hat{\boldsymbol{\tau}}) \,\mathrm{d}\boldsymbol{x} + \int_\Omega \operatorname{as}(\hat{\boldsymbol{\tau}}) \cdot \boldsymbol{r} \,\mathrm{d}\boldsymbol{x} \\
&\qquad - \int_{\Gamma_F} \boldsymbol{m}_s \cdot \big[T(\mathbf{n}_{\Gamma_F})(\hat{\boldsymbol{\tau}}\,\mathbf{n}_{\Gamma_F})\big] \,\mathrm{d}\boldsymbol{S} - \int_{\Gamma_D} \boldsymbol{u}_0 \cdot (\hat{\boldsymbol{\tau}}\,\mathbf{n}) \,\mathrm{d}\boldsymbol{s} \\
&\qquad + \int_\Omega (\nabla \cdot \boldsymbol{\sigma}) \cdot \hat{\boldsymbol{\omega}} \,\mathrm{d}\boldsymbol{x} + \int_\Omega \boldsymbol{f} \cdot \hat{\boldsymbol{\omega}} \,\mathrm{d}\boldsymbol{x} + \int_\Omega \operatorname{as}(\boldsymbol{\sigma}) \cdot \hat{\boldsymbol{\xi}} \,\mathrm{d}\boldsymbol{x} \\
&\qquad + \int_\Omega \frac{1}{2\mu(\boldsymbol{m}_\mu)} \big[\hat{\boldsymbol{\sigma}} - \frac{\nu}{1+\nu(d-2)} \operatorname{tr}(\hat{\boldsymbol{\sigma}})\boldsymbol{I}\big] : \boldsymbol{\tau} \,\mathrm{d}\boldsymbol{x} \\
&\qquad + \int_\Omega (\nabla \cdot \hat{\boldsymbol{\sigma}}) \cdot \boldsymbol{\omega} \,\mathrm{d}\boldsymbol{x} + \int_\Omega \operatorname{as}(\hat{\boldsymbol{\sigma}}) \cdot \boldsymbol{\xi} \,\mathrm{d}\boldsymbol{x} + \int_\Omega \operatorname{as}(\boldsymbol{\tau}) \cdot \hat{\boldsymbol{r}} \,\mathrm{d}\boldsymbol{x} \\
&\qquad + \int_\Omega \hat{\boldsymbol{u}} \cdot (\nabla \cdot \boldsymbol{\tau}) \,\mathrm{d}\boldsymbol{x} + \int_\Omega \mathcal{B}^* \boldsymbol{\Gamma}_{\text{noise}}^{-1} \big(\mathcal{B}\boldsymbol{u} - \mathbf{d}\big) \cdot \hat{\boldsymbol{u}} \,\mathrm{d}\boldsymbol{x}.
\end{aligned}
\tag{C.4}
$$

By taking the derivative of the second-order Lagrangian $\mathcal{L}^{\mathcal{H}}$ with respect to the adjoint variables $(\boldsymbol{\tau}, \boldsymbol{\omega}, \boldsymbol{\xi})$ we can solve the incremental forward equation to find the incremental state variables

$(\hat{\boldsymbol{\sigma}}, \hat{\boldsymbol{u}}, \hat{\boldsymbol{r}})$. The incremental forward problem reads:

$$
\begin{aligned}
&\left(\frac{\partial \mathcal{L}^{\mathcal{H}}}{\partial \boldsymbol{\tau}}, \tilde{\boldsymbol{\tau}}\right) + \left(\frac{\partial \mathcal{L}^{\mathcal{H}}}{\partial \boldsymbol{\omega}}, \tilde{\boldsymbol{\omega}}\right) + \left(\frac{\partial \mathcal{L}^{\mathcal{H}}}{\partial \boldsymbol{\xi}}, \tilde{\boldsymbol{\xi}}\right) \\
&\qquad = \int_{\Omega} \frac{\mu_m(\boldsymbol{m}_\mu)\hat{\boldsymbol{m}}_\mu}{2\mu^2(\boldsymbol{m}_\mu)} \left[\boldsymbol{\sigma} - \frac{\nu}{1+\nu(d-2)} \operatorname{tr}(\boldsymbol{\sigma})\boldsymbol{I}\right] : \tilde{\boldsymbol{\tau}} \, \mathrm{d}\boldsymbol{x} \\
&\qquad - \int_{\Gamma_F} \hat{\boldsymbol{m}}_s \cdot \left[T(\mathbf{n}_{\Gamma_F})(\tilde{\boldsymbol{\tau}}\, \mathbf{n}_{\Gamma_F})\right] \mathrm{d}\boldsymbol{S} \\
&\qquad + \int_{\Omega} \frac{1}{2\mu(\boldsymbol{m}_\mu)} \left[\hat{\boldsymbol{\sigma}} - \frac{\nu}{1+\nu(d-2)} \operatorname{tr}(\hat{\boldsymbol{\sigma}})\boldsymbol{I}\right] : \tilde{\boldsymbol{\tau}} \, \mathrm{d}\boldsymbol{x} \\
&\qquad + \int_{\Omega} \hat{\boldsymbol{u}} \cdot (\nabla \cdot \tilde{\boldsymbol{\tau}}) \, \mathrm{d}\boldsymbol{x} + \int_{\Omega} \operatorname{as}(\tilde{\boldsymbol{\tau}}) \cdot \hat{\boldsymbol{r}} \, \mathrm{d}\boldsymbol{x} \\
&\qquad + \int_{\Omega} (\nabla \cdot \hat{\boldsymbol{\sigma}}) \cdot \tilde{\boldsymbol{\omega}} \, \mathrm{d}\boldsymbol{x} + \int_{\Omega} \operatorname{as}(\hat{\boldsymbol{\sigma}}) \cdot \tilde{\boldsymbol{\xi}} \, \mathrm{d}\boldsymbol{x} = 0 \\
&\qquad\quad \forall \tilde{\boldsymbol{\tau}} \in \Sigma;\ \forall \tilde{\boldsymbol{\omega}} \in W;\ \forall \tilde{\boldsymbol{\xi}} \in \Xi.
\end{aligned}
\tag{C.5}
$$

The incremental adjoint equation is derived by taking the variation of $\mathcal{L}^{\mathcal{H}}$ with respect to the state variables $(\boldsymbol{\sigma}, \boldsymbol{u}, \boldsymbol{r})$ to find the incremental adjoint variables $(\hat{\boldsymbol{\tau}}, \hat{\boldsymbol{\omega}}, \hat{\boldsymbol{\xi}})$ reads:

$$
\begin{aligned}
&\left(\frac{\partial \mathcal{L}^{\mathcal{H}}}{\partial \boldsymbol{\sigma}}, \tilde{\boldsymbol{\sigma}}\right) + \left(\frac{\partial \mathcal{L}^{\mathcal{H}}}{\partial \boldsymbol{u}}, \tilde{\boldsymbol{u}}\right) + \left(\frac{\partial \mathcal{L}^{\mathcal{H}}}{\partial \boldsymbol{r}}, \tilde{\boldsymbol{r}}\right) \\
&\qquad = \int_{\Omega} \frac{\mu_m(\boldsymbol{m}_\mu)\hat{\boldsymbol{m}}_\mu}{2\mu^2(\boldsymbol{m}_\mu)} \left[\tilde{\boldsymbol{\sigma}} - \frac{\nu}{1+\nu(d-2)} \operatorname{tr}(\tilde{\boldsymbol{\sigma}})\boldsymbol{I}\right] : \boldsymbol{\tau} \, \mathrm{d}\boldsymbol{x} \\
&\qquad + \int_{\Omega} \frac{1}{2\mu(\boldsymbol{m}_\mu)} \left[\tilde{\boldsymbol{\sigma}} - \frac{\nu}{1+\nu(d-2)} \operatorname{tr}(\tilde{\boldsymbol{\sigma}})\boldsymbol{I}\right] : \hat{\boldsymbol{\tau}} \, \mathrm{d}\boldsymbol{x} \\
&\qquad + \int_{\Omega} \tilde{\boldsymbol{u}} \cdot (\nabla \cdot \hat{\boldsymbol{\tau}}) \, \mathrm{d}\boldsymbol{x} + \int_{\Omega} \mathcal{B}^* \boldsymbol{\Gamma}_{\text{noise}}^{-1} \mathcal{B} \tilde{\boldsymbol{u}} \cdot \hat{\boldsymbol{u}} \, \mathrm{d}\boldsymbol{x} \\
&\qquad + \int_{\Omega} \operatorname{as}(\tilde{\boldsymbol{\sigma}}) \cdot \hat{\boldsymbol{\xi}} \, \mathrm{d}\boldsymbol{x} + \int_{\Omega} (\nabla \cdot \tilde{\boldsymbol{\sigma}}) \cdot \hat{\boldsymbol{\omega}} \, \mathrm{d}\boldsymbol{x} \\
&\qquad + \int_{\Omega} \operatorname{as}(\hat{\boldsymbol{\tau}}) \cdot \tilde{\boldsymbol{r}} \, \mathrm{d}\boldsymbol{x} = 0 \\
&\qquad\quad \forall \tilde{\boldsymbol{\sigma}} \in \Sigma;\ \forall \tilde{\boldsymbol{u}} \in W;\ \forall \tilde{\boldsymbol{r}} \in \Xi.
\end{aligned}
\tag{C.6}
$$

Lastly, the expression of the Hessian action in a direction $(\tilde{\boldsymbol{m}}_\mu, \tilde{\boldsymbol{m}}_s)$ can be derived by taking the derivative of the second-order Lagrangian functional with respect to the model parameters $(\boldsymbol{m}_\mu, \boldsymbol{m}_s)$

to get:

$$\begin{aligned}\big((\tilde{\boldsymbol{m}}_\mu,\tilde{\boldsymbol{m}}_s),\, \mathcal{H}(\boldsymbol{m}_\mu,\boldsymbol{m}_s)\,(\hat{\boldsymbol{m}}_\mu,\hat{\boldsymbol{m}}_s)\big) &= (\tilde{\boldsymbol{m}}_\mu, \mathcal{R}_{mm}(\boldsymbol{m}_\mu)\,\hat{\boldsymbol{m}}_\mu) + (\tilde{\boldsymbol{m}}_s, \mathcal{R}_{mm}(\boldsymbol{m}_s)\,\hat{\boldsymbol{m}}_s)\\
&+ \int_\Omega \frac{\mu(\boldsymbol{m}_\mu)\,\mu_{mm}(\boldsymbol{m}_\mu) - \mu_m^2(\boldsymbol{m}_\mu)}{\mu^3(\boldsymbol{m}_\mu)}\,\tilde{\boldsymbol{m}}\hat{\boldsymbol{m}}\,\Big[\boldsymbol{\sigma} - \frac{\nu}{1+\nu(d-2)}\,\mathrm{tr}(\boldsymbol{\sigma})\boldsymbol{I}\Big] : \boldsymbol{\tau}\,\mathrm{d}\boldsymbol{x}\\
&+ \int_\Omega \frac{\mu_m(\boldsymbol{m}_\mu)\tilde{\boldsymbol{m}}_\mu}{2\mu^2(\boldsymbol{m}_\mu)}\Big[\boldsymbol{\sigma} - \frac{\nu}{1+\nu(d-2)}\,\mathrm{tr}(\boldsymbol{\sigma})\boldsymbol{I}\Big] : \hat{\boldsymbol{\tau}}\,\mathrm{d}\boldsymbol{x}\\
&+ \int_\Omega \frac{\mu_m(\boldsymbol{m}_\mu)\tilde{\boldsymbol{m}}_\mu}{2\mu^2(\boldsymbol{m}_\mu)}\Big[\hat{\boldsymbol{\sigma}} - \frac{\nu}{1+\nu(d-2)}\,\mathrm{tr}(\hat{\boldsymbol{\sigma}})\boldsymbol{I}\Big] : \boldsymbol{\tau}\,\mathrm{d}\boldsymbol{x}\\
&- \int_{\Gamma_F} \tilde{\boldsymbol{m}}_s \cdot \big[T(\mathbf{n}_{\Gamma_F})(\hat{\boldsymbol{\tau}}\,\mathbf{n}_{\Gamma_F})\big]\,\mathrm{d}\boldsymbol{S} \qquad \forall(\tilde{\boldsymbol{m}}_\mu,\tilde{\boldsymbol{m}}_s)\in\mathcal{M},\end{aligned} \tag{C.7}$$

where μ_m and μ_{mm} denote the first and second derivative of $\mu(\boldsymbol{m}_\mu)$ with respect to $\boldsymbol{m}_\mu$, respectively. $\boldsymbol{\sigma}$ and $\boldsymbol{\tau}$ are the solutions to the forward (eq. 3) and adjoint (eq. C.2) problems, respectively, and $\hat{\boldsymbol{\sigma}}$ and $\hat{\boldsymbol{\tau}}$ are the solutions of the incremental forward (eq. C.5) and adjoint (eq. C.6) problems, respectively.